John Rönn

Fabrication and characterization of atomic-layer-deposited Er_2O_3 for optical amplifier devices

School of Electrical Engineering

Thesis submitted for examination for the degree of Master of Science in Technology.

Espoo December 1, 2014

Thesis supervisor:

Prof. Zhipei Sun

Thesis advisor:

D.Sc. (Tech.) Lasse Karvonen

Aalto University
School of Electrical
Engineering

AALTO UNIVERSITY
SCHOOL OF ELECTRICAL ENGINEERING

ABSTRACT OF THE
MASTER'S THESIS

Author: John Rönn

Title: Fabrication and characterization of atomic-layer-deposited Er_2O_3 for optical amplifier devices

Date: December 1, 2014 Language: English Number of pages: 7+64

Department of Micro- and nanotechnology

Professorship: Micro- and nanotechnology Code: S3010

Supervisor: Prof. Zhipei Sun

Advisor: D.Sc. (Tech.) Lasse Karvonen

Recently, erbium-doped optical amplifiers have drawn significant attention as a solution to compensate the propagation losses for silicon photonics due to their ability to produce amplification of light at $\lambda = 1.5\,\mu$m with high efficiency and low noise over wide bandwidth. In silicon photonics, much effort has been put into the development of Er-doped optical amplifiers in the form of strip or slot waveguides, in which the amplification is produced over short ($\sim$ cm) structures. However, there has not been any major success in the development, because several challenges arise in Er-doped waveguide amplifiers as the amplification over short structures requires very high concentration of Er-ions in the amplifier gain material. It has been shown that some of these challenges can be avoided by optimizing the fabrication of the Er-doped gain material. Atomic layer deposition has shown a great potential in the fabrication of Er-doped materials because it can be used to precisely control the profile of the Er-ions in the amplifier gain material.
In this thesis, plasma-enhanced atomic layer deposition has been successfully used to fabricate Er-doped materials and to control their photoluminescence at $\lambda = 1.5\,\mu$m. This was done in two parts. First, an optimized ALD process for erbium in its sesquioxide form, Er_2O_3, was developed and as a result, a growth rate of 0.215 Å/cycle and non-uniformity of 3.55 % were obtained on 6" wafer. Er_2O_3 was then deposited in a nanolaminate configuration with Al_2O_3 and the thickness of the Al_2O_3 was controlled. The as-deposited samples were then optically characterized with absorption and photoluminescence measurements and it was observed that when the thickness of the Al_2O_3-layer between the Er_2O_3-layers was increased, an enhanced photoluminescence signal at $\lambda = 1.5\,\mu$m was measured. Therefore, this thesis shows that the photoluminescence of the Er-ions at $\lambda = 1.5\,\mu$m can be greatly enhanced by the nanoscale engineering of the fabrication process.

Keywords: Erbium, atomic layer deposition, optical amplifier, doping, photoluminescence, optical waveguide.

AALTO-YLIOPISTO
SÄHKÖTEKNIIKAN KORKEAKOULU

DIPLOMITYÖN
TIIVISTELMÄ

Tekijä: John Rönn

Työn nimi: Atomikerroskasvatetun Er_2O_3:n valmistaminen ja sen karakterisointi optisia vahvistinlaitteita varten

Päivämäärä: December 1, 2014 Kieli: Englanti Sivumäärä: 7+64

Mikro- ja nanotekniikan laitos

Professuuri: Mikro- ja nanotekniikka Koodi: S3010

Valvoja: Prof. Zhipei Sun

Ohjaaja: TkT Lasse Karvonen

Erbium-seostetut materiaalit ovat herättäneet kiinnostusta potentiaalisina materiaaleina valon vahvistamiseen ja valonlähteiksi piifotoniikassa. Piifotoniikassa valon teho vaimenee sekä sirujen välisissä kytkennöissä, että itse valokanavissa ja tämän takia signaalia täytyy vahvistaa. Myös halpojen, helposti integroitavien valonlähteiden puute on merkittävä ongelma piifotoniikassa. Jotta signaalin vavistus piipohjaisissa valokanavarakenteissa pystyttäisiin toteuttamaan, erbium-seostettuja materiaaleja on pyritty yhdistämään piifotoniikkaan. Valokanavissa törmätään kuitenkin erilaisiin haasteisiin, koska erbium-ionien määrää täytyy kasvattaa radikaalisti vahvistuksen aikaansaamiseksi lyhyillä matkoilla. Tästä syystä lisää tutkimusta ja uusia valmistustekniikoita tarvitaan erbium-pohjaisten valokanavavahvistimien toteuttamiseksi. Atomikerroskasvatusmenetelmä on erityisen potentiaalinen menetelmä erbium-pohjaisten materiaalien valmistamiseen, koska sillä voidaan tarkasti säätää erbium-ionien jakaumaa vahvistimen sisällä.
Tässä työssä on pystytty näyttämään, että plasma-avustettua atomikerroskasvatusmenetelmää voidaan käyttää erbium-seostettujen materiaalien valmistamisessa ja niiden optisten ominaisuuksien säätämisessä Al_2O_3-pohjaisissa näytteissä. Tämä tavoite saavutettiin kahdessa osassa. Ensimmäisessä osassa kehitettiin optimoitu prosessi erbiumoksidille (Er_2O_3). Kyseisen Er_2O_3-prosessin kasvunopeuden ja epätasaisuuden mitattiin olevan 0.215 Å/sykli ja 3.55 % kuuden tuuman kiekolla. Seuraavaksi alumiinioksidia seostettiin erbiumilla kasvattamalla Er_2O_3-kerroksia alumiinioksidikerrosten väliin. Materiaalin ominaisuuksia pystyttiin kontrolloimaan muuttamalla alumiinioksidikerroksen paksuutta Er_2O_3-kerroksen välillä. Optisissa mittauksissa huomattiin, että kun alumiinioksidikerroksen paksuus kasvoi, myös fotoluminesenssi 1.5 μm:n aallonpituudella kasvoi. Työ täten osoitti, että erbium-ionien fotoluminesenssiä voidaan tehostaa optimoimalla erbium-ionien valmistusmenetelmää.

Avainsanat: Erbium, atomikerroskasvatus, valovahvistin, douppaus, fotoluminesenssi, valokanava.

Preface

This thesis contains a lot of fabrication and characterization and therefore, many people have helped me during the process. First and foremost, I would like to thank my instructor Lasse Karvonen, who has not only instructed me in this thesis, but who has helped me with everything since the second year of my studies. I would also like to thank Sami Kujala and Seppo Honkanen, who instructed me in my Bachelor's studies intensively.

I would like to say many thanks to my advisor and professor, Zhipei Sun, who let me personally decide the topic of this thesis and who has backed up my decisions since he joined the Aalto University. I hope I can continue to work in Zhipei's group as a postgraduate student in the future.

In addition, special thanks are given to Antti Säynätjoki, who explained many things related to this thesis, to Henri Jussila and Jukka Hassinen who helped with with the optical measurements and to Alex Perros, Perttu Sippola and Ville Rontu who helped me with the ALD-processing.

Finally, I want to express my gratitude to my friends and family and to my beloved girlfriend Meri, to whom I fell in love during this thesis.

Otaniemi, December 1, 2014

Contents

Symbols and abbreviations

Symbols

E	Energy
ω	Angular frequency of light
ω_0	Resonance (center) frequency of light
λ	Wavelength (in general)
λ_c	Resonance (center) wavelength
λ_{exc}	Excitation wavelength
λ_{em}	Emission wavelength
$\Delta\lambda$	Bandwidth (FWHM)
$\hbar\omega$	Energy of a photon with angular frequency ω
σ_{21}	Emission cross-section
σ_{12}	Absorption cross-section

Abbreviations

EDFA	Erbium-doped fiber amplifier
EDWA	Erbium-doped waveguide amplifier
ALD	Atomic layer deposition
SE	Spontaneous emission
ASE	Amplified spontaneous emission
ETU	Energy-transfer up-conversion
CR	Cross-relaxation
ESA	Excited-state absorption
PL	Photoluminescence
NIR	Near-infrared
FWHM	Full-width at half-maximum
QM40	Quantamaster 40 fluorescence spectrometer

Materials

Er	Erbium
Er^{3+}	Erbium-ion (+3)
O_2	Oxygen
O_3	Ozone
H_2O	Water
Er_2O_3	Erbium oxide
Y_2O_3	Yttrium oxide
Al_2O_3	Aluminium oxide
a-Al_2O_3	Amorphous aluminium oxide
c-Al_2O_3	Crystalline aluminium oxide

1 Introduction

Light is electromagnetic radiation that can be found almost everywhere in the world. It is one of the most important physical phenomenom that can be used in various ways either in technology or simply in nature. In technology, one way to utilize light is to transfer information. Light travels as short pulses in optical networks where it is guided by optical fibers to its destination [1]. The core material of optical fibers is pure silica which can offer very low absorption to the signal light if the wavelength is chosen correctly. Modern telecommunication networks use $\lambda = 1.55\,\mu$m as the signal wavelength because the absorption of silica has its lowest value around this wavelength. This wavelength regime is often referred to as the third transparency window of silica [2]. In this transparency window, the attenuation is only limited by the Rayleigh scattering of light, as illustrated in Fig. 1 that shows the absorption spectrum of a commercial silica optical fiber [3]. The optical attenuation

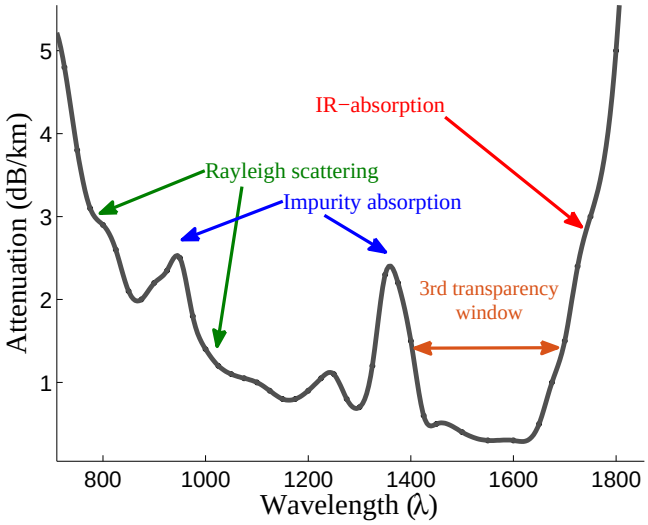

Figure 1: The attenuation spectrum of a commercial optical fiber. The attenuation is dominated by the Rayleigh scattering in the visible-NIR wavelengths and by optical absorption in the IR wavelengths. The attenuation is minimum at around $\lambda = 1.55\,\mu$m. Data from [3].

of this fiber can be made as small as 0.2 dB/km, which has enabled large amount of data to be sent in the optical networks. For example, today's internet connections can easily reach transfer rates of gigabits per second (Gbit/s) [4]. Moreover, the optical networks offer acceptable bit error rate even in large networks and they are nowadays used in long-distance telephone networks, high-density metropolitan areas and in cable-television trunk lines [5]. However, a problem rises in the large optical networks because the signal to be transferred still experiences moderate amount of loss (> 2 dB) after long-haul distances (> 10 km). The best solution to this problem is to use an optical amplifier which can compensate the losses that arise in these larger communication networks.

In photonics, there are three main types of optical amplifiers one can use to amplify light: rare-earth doped amplifiers, semiconductor amplifiers and Raman amplifiers [4]. Rare-earth doped amplifiers, especially rare-earth doped fiber amplifiers have been studied extensively because rare-earth elements possess unique optical properties [6]. When embedded in a proper host material, rare-earth ions can emit light with either very narrow or wide bandwidth in the visible and infrared spectrum [7]. Moreover, this emission can be controlled by the host material in which the rare-earth ions are doped [8]. Erbium (Er), which is one of the 17 rare-earth elements, has an emission band that coincides with the absorption minimum of commercial optical fibers. Because of this, much work has been put into the study of erbium as the gain material for the optical fiber amplifiers [5]. As a result, Er-doped fiber amplifiers (EDFAs) have been invented and they are nowadays a crucial part of the modern telecommunication networks [9].

Owing to the success of EDFAs, it is of great technological interest to bring the Er-doped amplifiers into micrometer sized photonic circuits that use light instead of electrical current to transfer information [10]. In photonics applications, especially in silicon photonics and integrated optics, most of the signal that travels in the optical waveguides is lost when the light is coupled into and between the integrated circuit chips. Therefore, Er-doped waveguide amplifiers (EDWAs) might enable new generation devices along with microelectronics because they can be used to amplify the light that is otherwise lost in the on-chip and chip-to-chip interconnects [11]. In future, this could possibly bring all the required functions of multiple optoelectronical devices into a single chip, thus, reducing the size and cost of modern optoelectronical systems greatly [12].

Although erbium has been widely studied in the association with optical fibers and fiber amplifiers, more knowledge is needed when the Er-doped amplifiers are integrated with optical waveguides. In the case of EDWAs, the amplification must be carried over much shorter lengths ($\sim$ cm), thus, requiring higher Er-ion concentrations than in the case of traditional fiber amplifiers in order to achieve reasonable amplification [13]. This brings two major challenges in the operation and fabrication of the EDWAs: First, typical glass materials cannot contain high concentration of Er-ions without clustering, and second, the ion-ion interactions create unwanted transitions that lead to reduced gain and increased noise in the Er-doped amplifier [14]. In order to answer these challenges and to ensure the best possible operation of the Er-doped waveguide amplifiers, the distribution of the Er-ions in the amplifier device has to be controlled. Therefore, a delicate care has to be invested in the fabrication technique of the Er-doped materials.

Er-doped materials can be grown using various methods, including atomic layer deposition [15], dip-coating [16], flame hydrolysis [17], high-vacuum chemical vapour deposition [18], plasma-enhanced chemical vapour deposition [19], pulsed laser deposition [20], reactive co-sputtering [21], RF-sputtering [22], sol-gel method [23], spin coating [24] and vapour phase deposition [25]. Of these fabrication methods, atomic layer deposition (ALD) is of the great interest because it possesses unique deposition properties that no other technique holds. For example, ALD is capable of producing thin films with very high conformality, aspect ratio and accurate

($\sim 99\,\%$) control of the film thickness [26]. Moreover, ALD also allows the nanoscale engineering of multifilm structures and the coating of low-loss waveguide structures with its sequential, self-limiting reactions [27, 28]. Thus, ALD offers a beneficial way to fabricate and to control the distribution of the Er-ions in the Er-doped host materials.

The fabrication of atomic-layer-deposited erbium in its sesquioxide form, Er_2O_3, has only been studied by few research groups [15, 29, 30, 31]. These reported studies have demonstrated that Er_2O_3 can be fabricated by using different erbium and oxygen source chemicals in the deposition. The choices for the source chemicals have been found to affect the growth rate of the Er_2O_3 significantly. For example, it has been reported that the precursor combination of $Er(thd)_3$ and O_3 yields a growth rate of 0.25 Å per cycle whereas the precursor combination of $Er(CpMe)_3$ and H_2O yields a growth rate of 1.5 Å per cycle. A general trend has been observed that the the use of water (H_2O) with thermally-driven ALD instead of ozone (O_3) leads to higher growth rates (> 1 Å/cycle). However, the growth conditions and the process parameters of the thermally-driven ALD processes are usually very limited when compared to plasma-assisted processes [32]. Plasma-enhanced ALD allows more freedom when choosing the deposition parameters and it usually leads to better material properties when compared to its thermal counterpart. Therefore, the fabrication of Er_2O_3 with plasma-assisted ALD has been chosen as the fabrication method in this thesis.

The purpose of this thesis is two-fold:

1. An ALD process development is performed for erbium in its sesquioxide form, Er_2O_3, using plasma-assisted ALD with tris(2,2,6,6-tetramethyl-3,5-heptanedionato) erbium and oxygen (O_2) plasma as the precursors. The goal is to perfect this fabrication process by optimizing each ALD-parameter one at a time in order maximize the growth and the uniformity of the deposited Er_2O_3 films. The main focus of this thesis is on this process development.

2. The optimized Er_2O_3 process is used with an already optimized Al_2O_3 process to fabricate Er_2O_3-Al_2O_3-nanolaminate structures in order to offer a suitable host material for the Er-ions and to increase the average distance between the adjacent Er-ions in the vertical direction. The reason behind this is that when the distance between the Er-ions increases, it reduces the unwanted transitions in the Er-doped material. After the fabrication, both the Er_2O_3 and Er_2O_3-Al_2O_3 samples are optically characterized with absorption and photoluminescence measurements in order to study the spectral response of Er_2O_3 in different compositions. Finally, the photoluminescence and absorption data are compared between the samples in order to see if the spectral response of the Er-ions can be enhanced with the nanoscale engineering of the fabrication process.

The structure of this thesis after this chapter is as follows: Chapter 2 gives an introduction to the optical amplification in order to understand how the amplification of light can be generated in Er-doped materials. Chapter 3 discusses the fundamentals of Er-doped optical amplifiers and their fabrication, in particular on the host

material selection. Chapter 4 focuses on the operation principle and properties of ALD and Chapter 5 describes the experimental tools that have been used in this thesis. Chapter 6 presents my results on the Er_2O_3 process development and in Chapter 7, my results from the optical measuements of the as-deposited Er_2O_3 and Er_2O_3-Al_2O_3 samples are presented and discussed thoroughly. Chapter 8 concludes this thesis with a brief summary as well as an outlook of the topic.

2 Optical amplification

The previous chapter explained why erbium is needed in the optical networks as a part of the amplifier design. In order to understand the physical phenomena behind these amplifiers and what exactly makes erbium so special material, it is mandatory to know how light can be generated and how it is amplified. Therefore, this chapter introduces the physical principles of the optical amplification and explains how it is generated in typical amplifier devices.

2.1 Classical model of optical amplification

The amplification of light is based on the interaction between light and matter. Einstein was the first to introduce a classical model that explained how light interacts with matter. He explained his theory by considering a two-level atom that includes an upper-level 2 with the energy E_2 and a lower-level 1 with the energy E_1. Einstein then proposed that there are three principle processes where light could interact with matter [33]. These are (see Figure 2):

1. Light absorption: An electron in the lower-level of the atom absorbs a photon that has energy of $\hbar\omega_{21} = E_2 - E_1$, where ω_{21} is the angular frequency of the photon. The electron is then excited to the upper level in the process. The probability for light absorption to occur is B_{12} and the rate is proportional to the number of atoms in the lower-level as well as to the energy density of the light.

2. Spontaneous emission: The electron that was excited to the upper-level can lose its energy by emitting a photon with angular frequency ω_{21} in a random direction. The electron then decays to the lower-level in the process. The probability for spontaneous emission to occur is A_{21} and the rate is only proportional to the number of excited atoms in the upper-level.

3. Stimulated emission: The energy of the electron in the upper-level can be stimulated by a photon with the energy $E_2 - E_1$. In this emission process, the electron decays to the lower-level by emitting a second photon with the same energy, phase, and direction as the incident photon. The probability for this process to occur is B_{21} and the rate is proportional to the number of excited atoms in the upper-level, as well as to the energy density of the light.

Einstein then argued that the third process, stimulated emission, lies in the heart of light amplification. The reason for this is simple: in the stimulated emission process, one photon enters the system, whereas two identical photons leave the system, and hence, amplification of light occurs. The probability parameters B_{12}, A_{21} and B_{21} are so called Einstein coefficients. Their precise values can be calculated using quantum mechanics if the wavefunctions of the energy levels of the atom are known [34].

Although stimulated emission is no doubt the most important of these three processes, the operation of optical amplifiers would not be possible without light absorption. Indeed, light absorption and stimulated emission processes can be closely

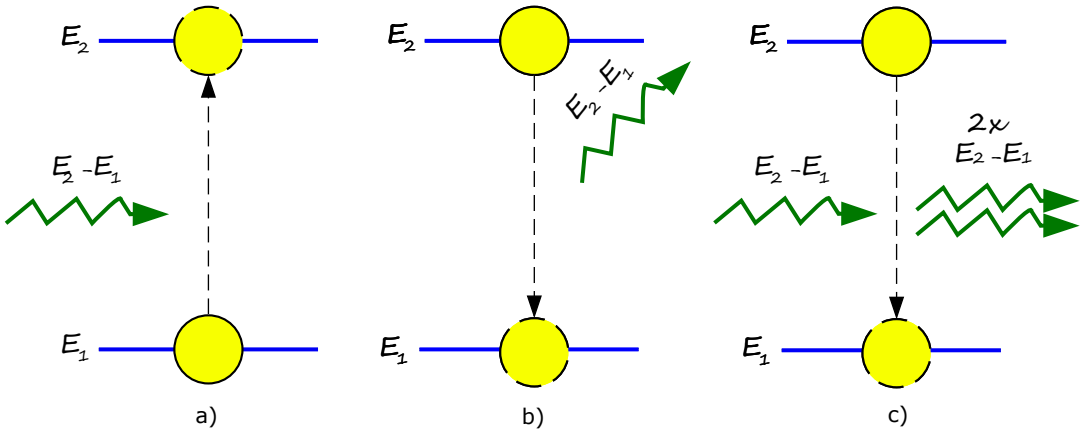

Figure 2: Interaction processes between light and matter; a) Light absorption, b) Spontaneous emission and c) Stimulated emission.

related to each another. It turns out that the probabilities for both processes to occur are equally likely, that is, $B_{21} = B_{12}$ if the upper- and lower-levels have the same degeneracy. This means that in normal conditions, the absorption and stimulated emission will compete against each other. Thus, the net gain or amplification is only dependent on the number of atoms in the upper- and lower-levels. [35]

The importance of light absorption in the operation of optical amplifier comes from the fact that naturally all the electrons in the atoms lie in the lowest-energy states, i.e. the probability of finding an electron in a high-energy state is lower than finding it in a low-energy state [33]. The probability function that describes the occupancy of the energy levels in a specific system is described by the Boltzmann distribution as given by Eq. 1 and shown in Fig. 3 [36]:

$$f(E) \propto \mathrm{e}^{-\frac{E}{kT}}. \tag{1}$$

From this one can see that the exponential behaviour of the occupation indicates

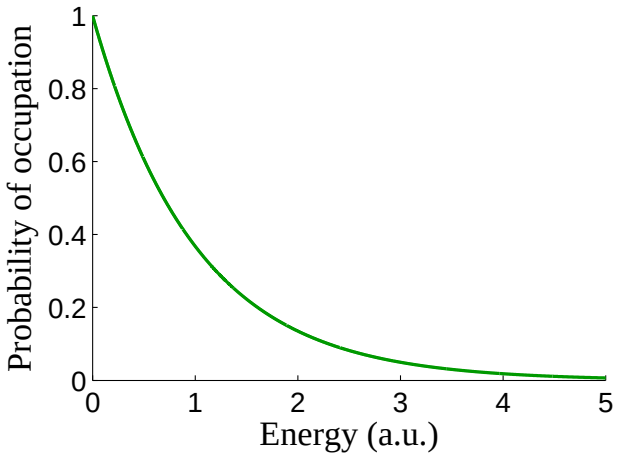

Figure 3: The Boltzmann distribution.

that the rate of stimulated emission will be vanishingly small in room temperature, because there are not enough excited atoms that can be stimulated to emit radiation. In order to increase the rate of stimulated emission to produce light amplification, the electrons must be excited to the upper level by an external pump source. The pumping is usually done optically, that is, using a laser source that excites the electrons by light absorption. Once the upper-level holds more electrons than the lower-level, the situation is called as population inversion [35]. The excited upper-level electrons can be then stimulated to produce photons and to realize light amplification.

2.2 3- and 4-level amplifiers

The principle operation of an optical amplifier is to produce gain. In a two-level atomic system that Einstein proposed, the amplification of light would occur when the rate of stimulated emission exceeded the rate of light absorption. This occurs when the number of atoms in the upper-level becomes higher than the number of atoms in the lower-level or in other words, when the population inversion is reached. It turns out that this kind of system cannot produce light amplification or gain, because the maximum number of excited atoms is half of the total number of atoms in the system [37]. The reason lies in the fact that when the number of atoms in the upper-level becomes equal to the number of atoms in the lower-level, the probability for stimulated emission to occur is half, whereas the probability of light absorption to occur is also half. That is, when atom is excited to the upper-level, the chance of releasing an electron from the upper-level is equally likely. Because of this, most lasers and amplifiers operate using so-called three- and four-level configurations [35].

Figure 4a shows the energy level schematic of a three-level amplifier. This configuration consists of three energy-levels: a ground state (1), a pump-level (3) and an upper-level (2). In equilibrium, the ground state holds most of the atoms, whereas the pump-level holds the lowest amount of atoms because of the Boltzmann statistics. In a working 3-level amplifier, the atoms are excited to the pump-level where they decay nonradiatively and very fast to the upper-level, creating population inversion between that level and the ground state. The lifetime of the upper-level is usually very long so that the population can build fast to achieve the population inversion. The excited atoms in the upper-level can be then released as stimulated emission to produce amplification for light that has energy equal to the energy difference between the upper-level and the ground state. The three-level amplifier has many advantages. First of all, in a three-level amplifier, the pump and signal lights have different wavelengths, thus, one avoids the re-absorption of the signal light to the upper-level. Secondly, the absorption spectrum of the pump transition is usually made very broad so that one can excite atoms in the ground state with spectrally wide pump sources [38].

Figure 4b shows an example of a 4-level amplifier. The configuration is almost same as in a 3-level amplifier except that there is now an additional level between the ground state and the upper-level. The atoms are first excited to the pump level (4), where they again decay nonradiatively and very fast to the upper-level (3). This

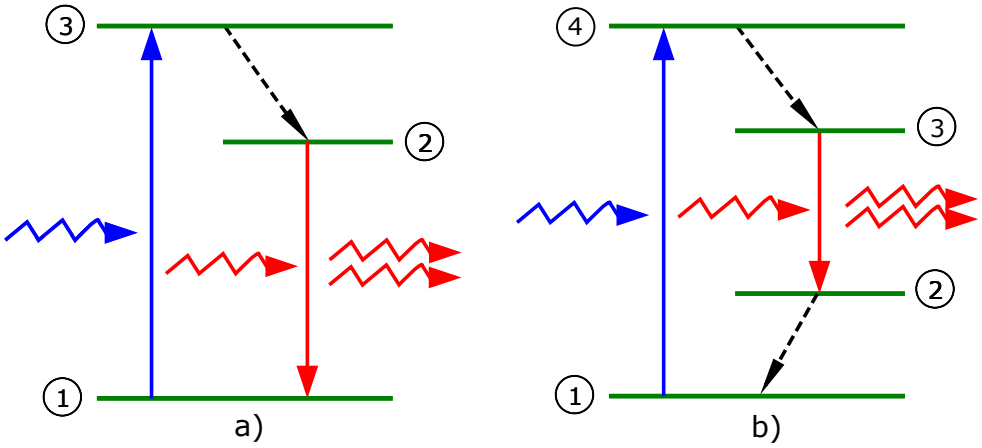

Figure 4: Energy level schematics of a) 3-level amplifier and b) 4-level amplifier. The blue arrows denote the pump light and the red arrows denote the signal light. In both figures, the dotted arrows express nonradiative transitions while the solid arrows express radiative transitions.

level has long lifetime in order to build up population on that level. The stimulated emission then occurs between the upper level and the lower level (2). The lower-level usually has very short lifetime so that the atoms can decay nonradiatively and very fast to the ground state, where they can be pumped to the pump level again. The advantage in a 4-level amplifier over a 3-level amplifier is the required number of excited atoms in the upper-level to reach the population inversion. In 4-level amplifier, the population inversion is reached very easily, because the lower-level is almost empty most of the time. Contrary, in 3-level amplifier, the lower-level is the ground state, which is heavily populated most of the time, thus, the population inversion is much harder to reach.

The whole operation of optical amplifier is based on the optical properties of the atom or ion that is used as the gain material in the amplifier. When designing an optical amplifier, it is mandatory to have knowledge on at least the following physical parameters of the gain medium:

1. Energy levels of the gain material
2. Lifetimes of the energy levels
3. Optical cross-sections between each levels
4. Spectral reponses of the allowed transitions
5. Available pump sources
6. Thermal endurance of the gain material
7. Suitable host material for the gain material

Of course, it is not easy to fulfill all the required criteria for the gain material, especially when one has to consider the rarity, price and fabrication of the material also. The energy-levels of suitable gain materials may not support the 4-level amplifier configuration so one has to settle for a 3-level amplifier which requires much larger amounts of pump powers to produce gain. All in all, it is up to the engineer to choose which parameters are important for specific applications.

3 Erbium in optical amplifiers

The previous chapter introduced the basic principles of optical amplification and demonstrated how it is generated in optical amplifiers. This chapter presents erbium as a gain material for the optical amplifiers and explains what makes erbium so unique material in the optical applications. In section 3.1, the atomic configuration of erbium is reviewed in order to understand its unique optical properties. The energy levels of erbium and the allowed transitions in the Er-ions are also presented. Section 3.2 introduces the operation principle of the Er-doped amplifiers and Section 3.3 gives a detailed analysis on the detrimental effects that limit the operation of these amplifiers. Finally, section 3.4 focuses on the fabrication of Er-doped materials and gives the requirements for the host materials that need to be satisfied in order to produce functional Er-doped amplifier materials.

3.1 Optical properties of erbium

Erbium is a rare-earth metal that belongs to the group of lanthanides [39]. The lanthanide group consists of elements with atomic numbers from 57 to 71 as shown in Figure 5, which presents the periodic table of elements. First lanthanide is lan-

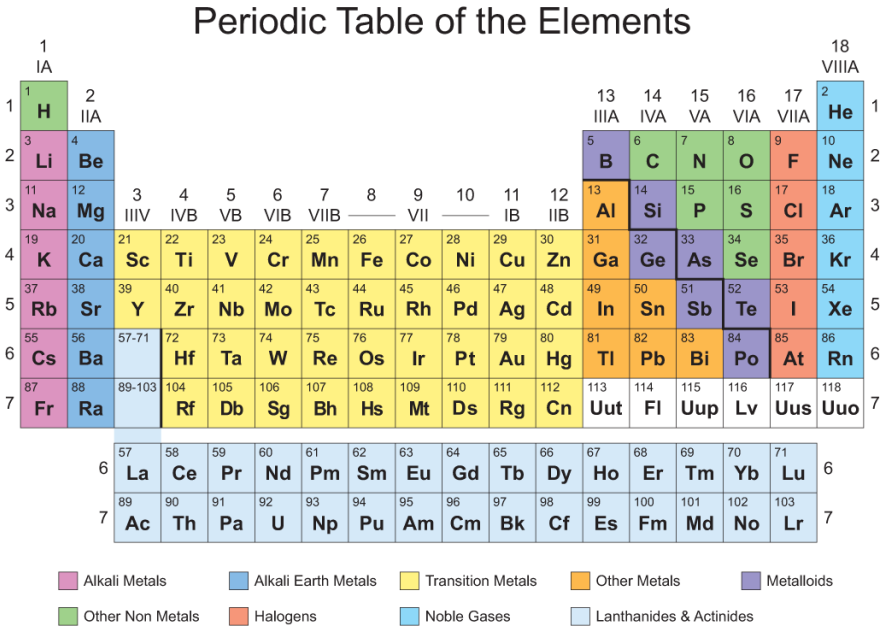

Figure 5: The periodic table of the elements that shows the group of the lanthanides. [40]

thanum, then cerium and so on. The most interesting elements in this category for optical devices are neodymium (Nd - 60), erbium (Er - 68) and ytterbium (Yb - 70). It is worthwhile to note that rare-earth elements are actually not so rare; most elements can be found in earth's crust in moderate amounts [9]. Erbium was first discovered near the village of Ytterby by Carl Gustaf Mosander in 1843. Mosander named one of the rare-earth elements, ytterbium, after this village and gave erbium

its name accordingly. Erbium and other rare-earth elements cannot be found alone; they are always part of some minerals and their extraction has been very difficult and expensive until ion-exchange methods were produced [9].

Erbium and the other lanthanides are interesting materials both physically and chemically because their atomic properties are different from those of semiconductors or transition metals. This can be explained with their electronic configuration. In the classical model of atoms the atom consists of positive nucleus surrounded by negatively charged electrons. When the atomic number Z increases, the electron shells with the lowest energies are filled first and the shells with the highest energies are filled last. In principle, these shells have increasing radii as one moves from the inner shell all the way to the outer shell. However, starting from the element with the atomic number $Z = 57$, that is, the first rare-earth metal lanthanum, the radii of the highest-lying energy shells actually shrink and cannot obey this rule anymore [9]. To gain insight what exactly happens inside lanthanides when the radii of the outer shells start to shrink, take, for example, the electronic configuration of erbium:

$$1s^2 2s^2 2p^6 3s^2 3p^6 3d^{10} 4s^2 4p^6 4d^{10} 5s^2 5p^6 4f^{12} 6s^2$$

or $[Xe]4f^{12}6s^2$ where [Xe] presents the core of the element xenon. The energy states are labeled using the spectroscopic notation [33]. The principal quantum number is given first, followed by the orbital quantum number as letter and the power denotes how many electrons the specific state holds. Table 1 shows which letter matches the orbital quantum number, l, in the above notation. Nevertheless, erbium alone

Table 1: Orbital quantum number in spectroscopic notation.

Letter	s	p	d	f	g	h	i
l	0	1	2	3	4	5	6

is almost always found in its trivalent state, Er^{3+}, because its 6s electrons and one 4f electron are usually removed due to their low ionization energies. The electronic configuration of Er^{3+} is $[Xe]4f^{11}$, thus, the electrons in the 4f state are the valence electrons of the Er-ion, that is, they have the highest energy and they are responsible for the chemical bonding of the element. However, it turns out that the average radius of this 4f orbital is almost twice as small as the average radii of the fully-occupied 5s and 5p orbitals [9]. This means that the valence electrons in the 4f state penetrate deep in to the core of erbium and are, thus, shielded by the 5s and 5p electrons [6]. As a consequence, the valence electrons cannot participate in chemical reactions. This is the main reason why lanthanides have their own group in the periodic table of the elements.

The shielding of the valence electrons gives erbium and the other lanthanides rich optical properties that can be employed in the optical applications. In order to undestand where these unique optical properties of erbium and the other lanthanides come from, let us take a closer look how a series of interaction processes lead to the generation of energy levels in the Er-ions, as illustrated in Figure 6:

1. The 4f energy state that holds 11 electrons is actually a combination of $2l+1$ degenerate energy levels, which corresponds to 7 degenerate energy states in the 4f shell. Each of these levels can hold two electrons; one spin-up electron and one spin-down electron.

2. The degeneracy of the 4f level is hardly maintained because the atomic interactions, such as spin-orbit, orbit-orbit, spin-spin and residual electrostatic interactions between the individual electrons break the degeneracy of the energy states [38], resulting in 7 nondegenerate sub-energy levels within the 4f shell of Er^{3+}. However, the electronic transitions within these sublevels are forbidden in Er^{3+} because the wavefunctions of the energy states have same parity.

3. When the Er-ions are doped into a solid host, the 5s and 5p electrons shield the 4f valence electrons from the crystal field that arises from the solid environment [9]. Thus, the interaction between the crystal field and the atomic interactions is weak so that the original sub-energy states within the 4f shell are changed only slightly. At the same time, the parity of the wavefunctions is broken by the crystal field, because the shielding provided by the 5s and 5p orbitals is not ideal. Thus, the electronic transitions within the 4f shell become weakly allowed [6]. Due to nature of these weak transitions, the radiative lifetimes of the energy levels are long and the corresponding linewidths of the transitions very sharp [38].

4. The solid host material, in which the Er-ions are doped, also causes the splitting of the 4f energy sublevels due to the Stark effect, creating small energy bands that broadens the emission and absorption spectra of the Er-ions to some degree [41].

The shielding of the valence electrons from the crystal field of the solid is very unique because the spectral response of the Er-ions is almost independent of the solid host material in which the ions are doped. This is also true for the other lanthanides. In semiconductors and transition metals, the electrons are given to the solid mutually, allowing the wavefunctions of these electrons to become very delocalized [36]. Thus, the emission and absorption spectra of the lanthanides are much sharper than those of semiconductors or transition metals. This is the main reason why rare-earth metals are used in optical amplifiers and lasers.

Figure 7 shows the seven lowest energy bands and their lifetimes in Er-doped silica glass [13]. The original energy levels in a free Er-ion are now split into energy bands due to the Stark effect arising from the crystal field of the glass material. The number of energy levels generated in the specific band is given by $(2J+1)/2$, where J is the total angular momentum of the state [9]. For example, the first excited state, $I_{13/2}$, is split into 7 energy levels. The energy bands are labeled using the Russel-Saunders notation ${}^{2S+1}L_J$, where S is the total spin quantum number of the state, L the total orbital quantum number of the state and J the total angular momentum $\vec{J} = \vec{L} + \vec{S}$ of the state [34]. The 6th energy band consists of two states,

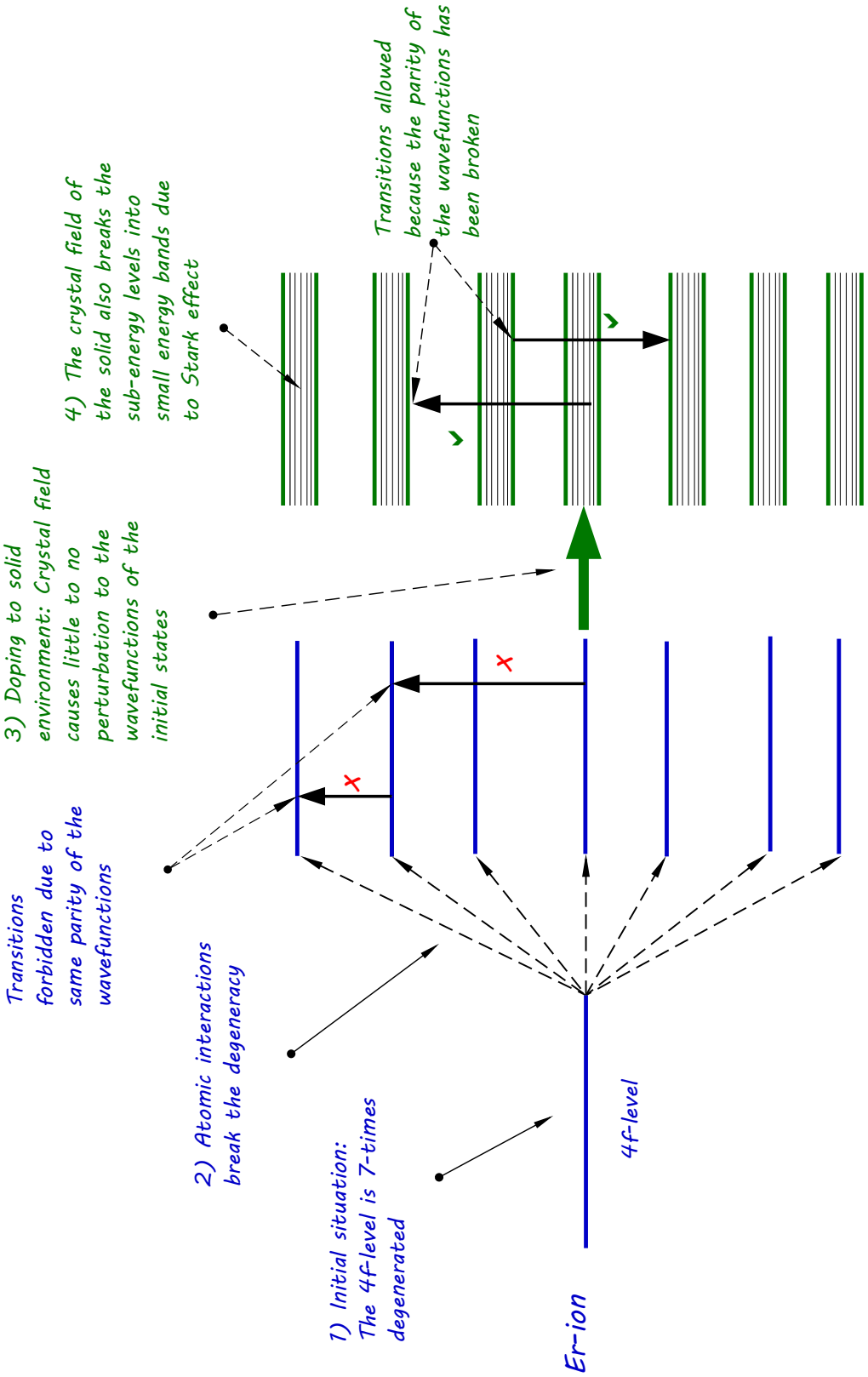

Figure 6: The generation of energy levels in Er^{3+} (blue) and Erbium-doped host material (green).

$^4S_{3/2}$ and $^2H_{11/2}$. Of course, the structure of the bands depends on the composition of the host material. For example, the imperfections and local variations in the solid usually cause deviations in the crystal field, which affects the energy levels of the active ions. However, this variation is usually small so that the central wavelengths of the transitions remain unchanged.

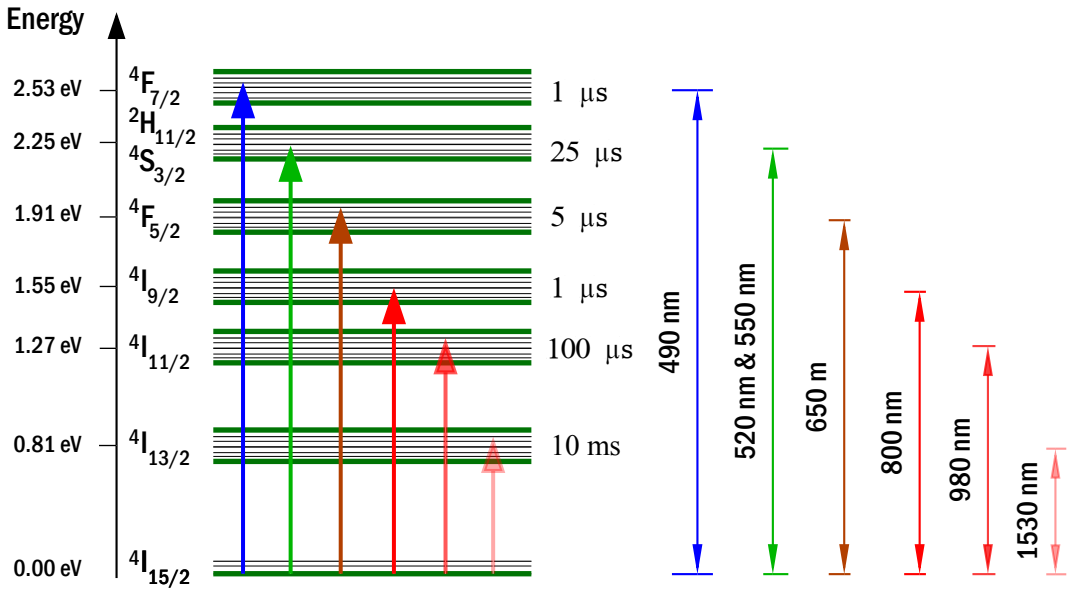

Figure 7: The seven lowest energy bands and their characteristic parameters in Er-doped silica glass.

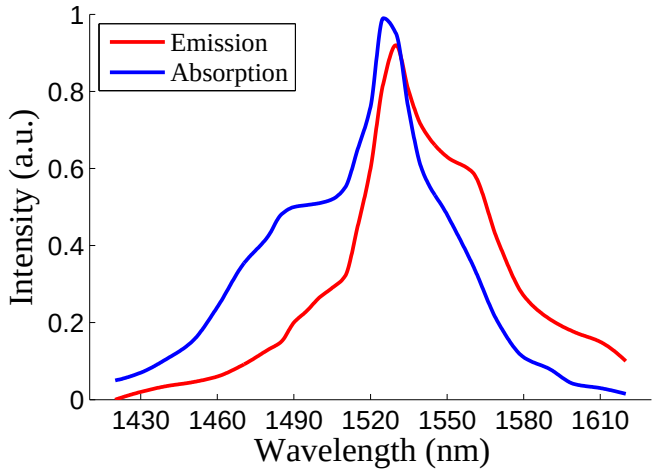

Figure 8: Absorption and emission spectra of the $I_{15/2} \leftrightarrow I_{13/2}$ transition in Er-doped silica glass. Data from [11].

In Fig. 7, one can distinguish the most important transition $I_{15/2} \leftrightarrow I_{13/2}$ which corresponds to a wavelength of 1530 nm. This transition is used in all the Er-doped

optical amplifiers to amplify the signal that is transmitted in the optical networks. The absorption and emission spectra of this transition are shown in Fig 8. In this figure, it can be observed that the spectra are rather wide. This is because there are a total of 56 allowed transitions between the first excited state $I_{13/2}$ and the ground state $I_{15/2}$ due to the Stark effect generated by the glass host. The peak values of the emission and absorption cross-sections are on the order $10^{-20} - 10^{-21}\,\mathrm{cm}^2$, which are small compared to the other types of gain media [38]. The reason for this is the weakly allowed transitions in the Er-ions due to the parity-forbidden nature of the energy levels within the 4f orbital. [9].

3.2 Erbium-doped optical amplifiers

In the previous section, the optical properties of erbium were demonstrated and the most important transition in Er^{3+} was mentioned. It was also demonstrated that no emission of light could occur in a free Er^{3+}-ion. Therefore, the Er-ions require a host material where they can be doped. When doped to a suitable host material, there are also several other relevant transitions in Er^{3+} that are important when it comes to the design of Er-doped amplifiers. The purpose of this section is to focus on these transitions as well as on the whole operation of Er-doped amplifiers.

Figure 7 shows that in a typical Er-doped amplifier, it is possible to pump the ground state electrons into the upper bands with various pump lasers. One can use, for example, Ar laser ($\lambda_c = 488\,\mathrm{nm}$) for the $I_{15/2} \rightarrow F_{7/2}$ excitation, frequency-doubled Nd-YAG laser ($\lambda_c = 532\,\mathrm{nm}$) for the $I_{15/2} \rightarrow S_{3/2}, H_{11/2}$ excitation, Kr laser ($\lambda_c = 647.1\,\mathrm{nm}$) for the $I_{15/2} \rightarrow F_{5/2}$ excitation, Ti-sapphire laser ($\lambda_c = 800\,\mathrm{nm}$) for the $I_{15/2} \rightarrow I_{9/2}$ excitation, and InGaAs and InGaAsP diode-lasers for the $I_{15/2} \rightarrow I_{11/2}, I_{13/2}$ excitations, respectively.

When the Er-ions are excited to any of these upper energy bands, they usually decay nonradiatively to the first excited state, which starts to populate because of the very long lifetime (10 ms) of that level. This is demonstrated in Fig. 9a. The nonradiative transitions occur as either single- or multi-phonon absorptions because the phonon energies are usually high in most suitable host materials in which the Er-ions are doped [35]. The amplification of the signal light can be then realized between the first excited state and the ground state to produce photons with wavelenghts around $\lambda = 1.53\,\mu\mathrm{m}$.

However, in order to maximize the number of the excited ions and hence, the gain of the amplifier, it is recommended to use either the $I_{15/2} \rightarrow I_{13/2}$ or the $I_{15/2} \rightarrow I_{11/2}$ transition [1]. When one of these pumping configurations is used, the amplifier operates as a 3-level amplifier as shown in Figs. 9b and 9c. With the pump wavelength of 980 nm, the ground-state electrons are excited to the $I_{11/2}$ band where they decay nonradiatively to the $I_{13/2}$ band. Because of the short lifetime of the $I_{11/2}$ band and long lifetime of the $I_{13/2}$ band, one can easily produce population inversion between the ground state and the first excited state.

Although the $I_{15/2} \rightarrow I_{13/2}$ pump configuration includes only two energy bands, it is possible to pump the ground state electrons into the upper part of the $I_{13/2}$ band, where they can decay nonradiatively to the lower part of the band, from which

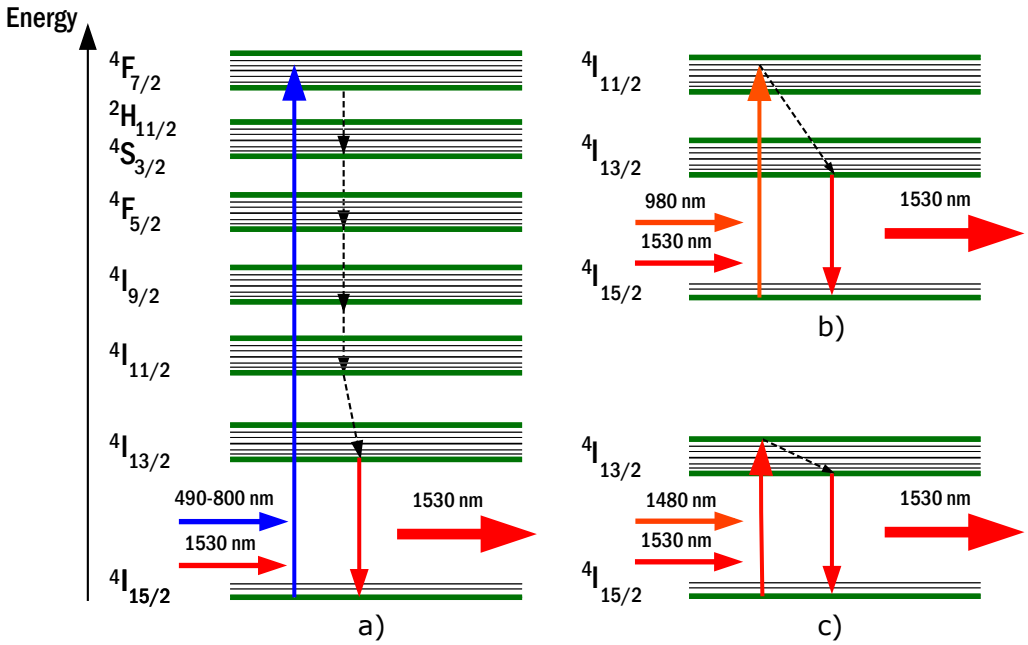

Figure 9: The operation principle of Er-doped amplifier with the pump sources operating at a) $\lambda = 490/520/550/650/800\,\text{nm}$; b) $\lambda = 980\,\text{nm}$ and c) $\lambda = 1480\,\text{nm}$. In a), the blue light is the pump light and the red light is the signal light whereas in b) and c), the orange light is the pump light and the red light is the signal light. The upward arrows express absorption while the downward arrows express emission. The dotted arrows express nonradiative transitions due to single- or multi-phonon absorption.

they can be then stimulated to produce amplification [4]. This is illustrated in Fig. 9c, where the pump wavelength has been chosen to be 1480 nm, which is widely used in Er-doped fiber amplifiers [3, 4]. Pumping with either $\lambda = 980\,\text{nm}$ or $\lambda = 1480\,\text{nm}$ is not only beneficial because of the efficiency, but also due to the fact that both of these pump wavelengths can be accessed with diode lasers.

In order to get some insight on the structure of the real Er-doped amplifiers, Figure 10 shows two devices that use erbium as the gain medium for the amplification of light: EDFA and EDWA [11]. In EDFA, the core material is typically Er-doped silica (SiO_2), which serves not only as the amplifier, but also as the optical waveguide for the signal light. In this fiber, a portion of the core is doped with Er-ions which are pumped with an external light source. The pump light travels inside the whole fiber as multimode in order to maximize the input coupling. The signal light, in turn, travels inside the fiber core where it stimulates new photons in the Er-doped core material, allowing the signal light to get amplified. The core then guides the amplified light outside the fiber to specified purposes.

Figure 10b shows the structure of EDWA. The core in this waveguide configuration is usually Er-doped Al_2O_3, Y_2O_3 or other suitable host material that guides the light due to the index guiding [12]. The core of the waveguide is doped with

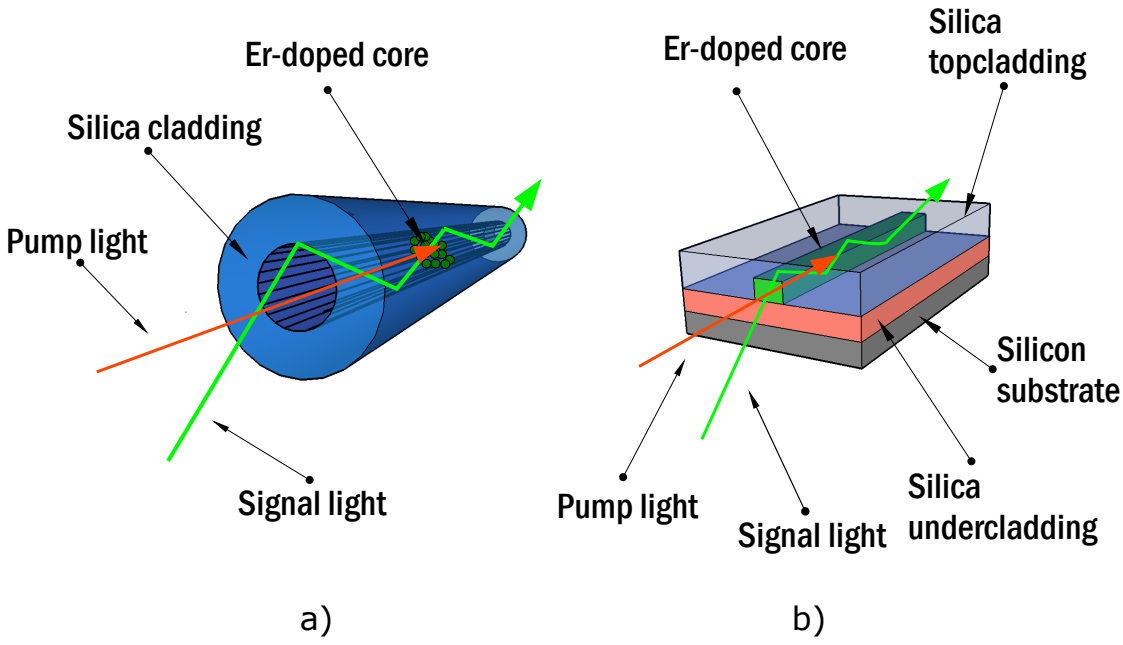

Figure 10: Typical structure of a) Er-doped fiber amplifier and b) Er-doped waveguide amplifier.

very high concentration of Er-ions and it is placed between top- and undercladding made of silica or other cladding material that has lower refractive index. The device itself is usually fabricated on top of silicon.

3.3 Detrimental transitions in Er-ions

Besides the transitions shown in Figures 7 and 9, there are also other important transitions that usually limit the operation of the Er-doped amplifiers. These unwanted transitions occur when the excited ions interact with either light or other neighboring ions before they are stimulated. The transitions can be divided into two categories: the ones that excite the ions into the upper-energy bands of the amplifier and the ones that occur when the ions decay from these upper-energy bands and generate light that is out-of-phase or has different wavelength than the signal light that needs to be amplified. The former category is also known as the up-conversion of light.

3.3.1 Up-conversion of light

Up-conversion is, by definition, a process in which the sequential absorption of two or more photons leads to the emission of light at shorter wavelength than the excitation wavelength [6]. Up-conversion is an unwanted process in the operation of Er-doped amplifiers at $\lambda = 1.53\,\mu$m, but it can be efficiently used in other amplifiers and optical applications to generate light that cannot be generated via other means

or the generation is much easier by using longer wavelength pump sources. Up-conversion has found many applications in the medical industry where the generation of light at visible wavelengths from near-infrared (NIR) light sources have been used, for example, in bioimaging [42]. Up-conversion of light can occur either as energy transfer between adjacent the Er-ions or when the excited Er-ions absorb one or more photons before relaxing to the ground state [5]. The former of these is known as the *energy-transfer up-conversion* (ETU) and the latter is known as the *excited state absorption* (ESA).

In ETU process, two nearby-lying excited ions exchange energies so that one ion gains the energy of both ions. The ion that loses its energy (donor) decays to one of the lower-levels, while the ion that gains the energy (acceptor) excites to one of the upper-energy bands. In Er^{3+}, there are two ways for the energy-transfer up-conversion process to occur [11]. These can be expressed with the following equations:

$$\begin{aligned} \mathrm{Er}^{3+}\left(\mathrm{I}_{13/2}\right) + \mathrm{Er}^{3+}\left(\mathrm{I}_{13/2}\right) &\rightarrow \mathrm{Er}^{3+}\left(\mathrm{I}_{11/2}\right) + \mathrm{Er}^{3+}\left(\mathrm{I}_{15/2}\right) \quad (2) \\ \mathrm{Er}^{3+}\left(\mathrm{I}_{11/2}\right) + \mathrm{Er}^{3+}\left(\mathrm{I}_{11/2}\right) &\rightarrow \mathrm{Er}^{3+}\left(\mathrm{I}_{15/2}\right) + \mathrm{Er}^{3+}\left(\mathrm{F}_{7/2}\right) \quad (3) \end{aligned}$$

In the first case (ETU1), the up-conversion occurs between two ions in the first excited state $\mathrm{I}_{13/2}$. The acceptor ion excites to the $\mathrm{I}_{11/2}$ state while the donor ion decays to the ground state $\mathrm{I}_{15/2}$. The outcome is the loss of two excited ions in the $\mathrm{I}_{13/2}$ state that could have been stimulated to produce amplification of light. Thus, the process leads to the reduction of gain in the amplifier [11]. In the second case (ETU2), the up-conversion occurs in the second excited state $\mathrm{I}_{11/2}$ where the ions are pumped when using $\lambda = 980\,\mathrm{nm}$ pump wavelength. In ETU2, the acceptor ion excites to the $\mathrm{F}_{7/2}$ state while the donor ion decays to the ground state. Although this process does not reduce the number of excited ions in the first excited state directly, it reduces the pump efficiency of the amplifier because the excited ions are lost from the $\mathrm{I}_{11/2}$ state [13].

In ESA, the ions that have already been excited to the upper-bands by the pump light can excite again by absorbing a second pump photon in the process. In the Er-ions, ESA usually occurs with 980 nm pumping in the following way [6]:

$$\begin{aligned} \mathrm{Er}^{3+}\left(\mathrm{I}_{15/2}\right) + \hbar\omega &\rightarrow \mathrm{Er}^{3+}\left(\mathrm{I}_{11/2}\right), \\ \mathrm{Er}^{3+}\left(\mathrm{I}_{11/2}\right) + \hbar\omega &\rightarrow \mathrm{Er}^{3+}\left(\mathrm{F}_{7/2}\right), \end{aligned} \quad (4)$$

where $\hbar\omega$ is the energy of the photon produced by the 980 nm pump source. Thus, the process excites a ground state ion to the pump band $\mathrm{I}_{11/2}$, where it is excited again to the $\mathrm{F}_{7/2}$ band. The outcome is the loss of two photons, that is, reduced pump efficiency [6].

3.3.2 Spontaneous transitions

When the Er-ions in the amplifier are excited to the upper-energy bands via the transitions generated by the up-conversion processes, the ions can decay radiatively or nonradiatively to the lower-energy bands. When the energy difference between

the excited state of the ions and the lower-lying state is small, the transition occurs nonradiatively [36]. In nonradiative transition, the energy is lost to phonons which results as the heating of the crystal. However, if the energy difference is sufficiently high and the phonon energies of the host material low, the transition occurs radiatively [35]. In radiative transition, the energy is lost to spontaneously emitted photons which have random phase and energy corresponding to the energy difference between the energy states of the transition. Thus, *spontaneous emission* (SE) leads to a noise in the amplifier. In general, there is always spontaneous emission present when the Er-ions are excited. Spontaneous emission usually occurs between unstable and metastable states [9]. Thus, in the Er-ions, the destination of spontaneous emission is most likely the ground state or the first excited state. If spontaneous emission is generated between the first excited state and the ground state, the amplifier can amplify these spontaneously emitted photons. This process is known as the *amplified spontaneous emission* (ASE) and it usually reduces the gain and leads to additional noise in the amplifier [3].

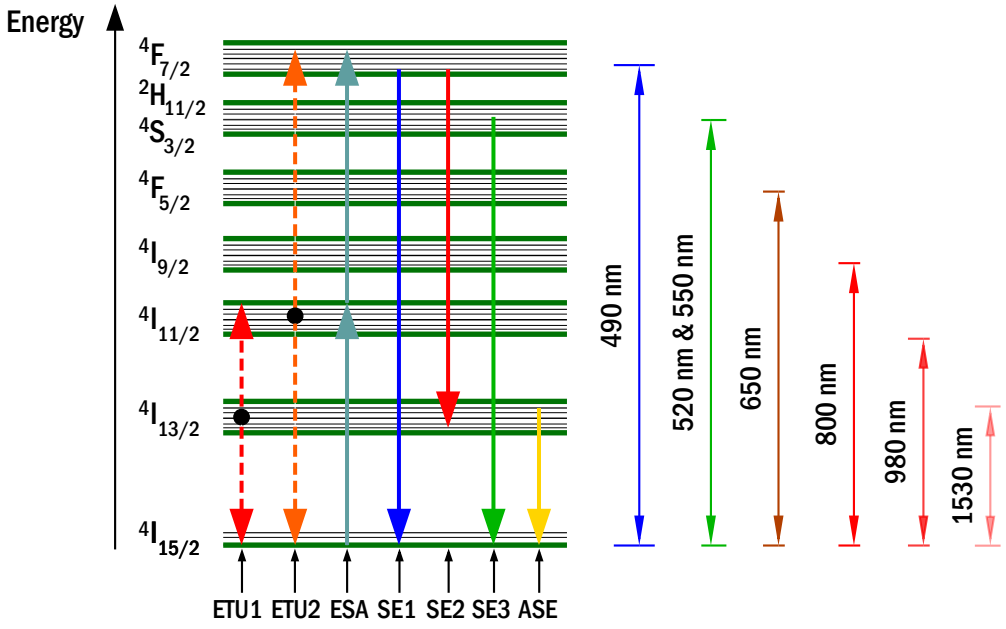

Figure 11: The detrimental processes in the operation of Er-doped amplifiers. The processes from left to right are: energy-transfer up-conversion (ETU), excited-state absorption (ESA), spontaneous emission (SE) and amplified spontaneous emission (ASE).

When up-conversion of light occurs via the ETU2 and ESA processes described in the previous subsection, the Er-ions excite to the $F_{7/2}$ state. Because the $F_{7/2}$ state has short lifetime and only slightly higher energy than the lower-lying energy state $H_{11/2}$, the Er-ions can decay either nonradiatively or radiatively from this state. If the transition occurs radiatively, then the Er-ions decay either to the first excited state $I_{13/2}$ or to the ground state $I_{15/2}$. As a result, the spontaneously

emitted photons have wavelength of either $\lambda = 490\,\text{nm}$ (SE1) or $\lambda = 720\,\text{nm}$ (SE2), which correspond to the transitions $F_{7/2} \rightarrow I_{15/2}$ and $F_{7/2} \rightarrow I_{13/2}$, respectively. If the transition occurs nonradiatively, then the electrons decay to the lower-lying energy state $H_{11/2}$ without emitting photons in the amplifier. However, the energy difference between this state and the lower-lying state $F_{5/2}$ is now higher and the transition from the $H_{11/2}$ state occurs radiatively and most likely to the ground state, generating light with wavelength of $\lambda = 520\,\text{nm}$ (SE3). This charasteristic green light is observed in most Er-doped gain materials that operate with the pump wavelength of $\lambda = 980\,\text{nm}$ [43, 44].

Thus, multiple wavelengths that have shorter wavelength than the pump wavelength are usually generated in Er-doped amplifiers. Moreover, the probability for these up-conversion processes increase when one increases the pump power or the density of the Er-ions in the gain medium [6]. The detrimental transitions discussed in this section are summarized in Figure 11.

3.4 Fabrication of Er-doped materials

In the previous section, the detrimental processes which limit the operation of the Er-doped amplifiers were discussed in detail. It turns out that some of these unwanted processes can be avoided or reduced by fabricating the erbium-doped gain material properly. Therefore, the topic of this section is to present how erbium-doped gain material should be fabricated and what host materials are suitable for the Er-ions in order to produce amplifiers with as high gain and low noise as possible.

3.4.1 Suitable host materials

There are several requirements for the host material that need to be satisfied in order to produce functional amplifier devices. These are listed below [11]:

1. *Suitable structure for the Er-ions.* The host material must posses noncentrosymmetric bonding sites for the Er-ion in order to break the parity of the wavefunctions of the energy states, allowing transitions within the 4f-shell. Furthermore, the lattice position has to be large enough to create sufficient distance between the adjacent Er-ions. Because the oxidation state of Er^{3+} is $+3$, the ions form sesquioxides Er_2O_3 with oxygen. Therefore, other sesquioxides with approximately the same cationic radii are suitable host materials. These include, for example, Y_2O_3 [30], a-Al_2O_3 [45] and Lu_2O_3 [46].

2. *High Er-solubility.* The host material should possess the ability to be doped with high concentration of Er-ions without clustering. This is mandatory in shorter amplifier devices, because the gain that the amplifier can provide is proportional to

$$G \propto \exp\left[L\left(\sigma_{21}(\lambda)N_2(z) - \sigma_{12}(\lambda)N_1(z)\right)\right], \tag{5}$$

where L is the amplifier length, N_2 and N_1 the number of ions in the upper- and lower-level, respectively, and σ_{21} and σ_{12} are the emission and absorption cross sections, respectively [5]. From Eq. 5, one can see that the gain

is exponentially-dependent on the product of the device length, the number of Er-ions in the upper- and lower-levels, and the magnitudes of the cross-sections. Because one cannot change the values of the cross-sections dramatically, the amount of active Er-ions should be made higher when the device length becomes shorter. For example, the density of the active Er-ions in a typical fiber amplifier is approximately $10^{17} - 10^{18}\,\mathrm{cm}^{-3}$ so that a reasonable amplification is achieved over several meters [47]. However, when the amplifier is implemented in centimetre-sized devices, the density of the active ions should reach the orders of $10^{20} - 10^{21}\,\mathrm{cm}^{-3}$ [12]. When the amount of active ions becomes this high, the ion-ion interactions start to play an important role in the amplifier. Therefore, the active ions should not cluster inside the host material.

3. *Long radiative lifetime of the $I_{13/2}$ level.* The host material should be able to offer long radiative lifetime of the first excited state in order to populate the $\mathrm{I}_{13/2}$ level quickly and to produce population inversion in the amplifier.

4. *Low phonon energy.* The phonon energy of the amplifier is completely determined by the host material. The host material should have low phonon energies in order to prevent the nonradiative transitions between the first excited state and the ground state.

5. *High purity.* As was stated in the previous chapter, the local variations and impurities affect the absorption and emission spectrum. Therefore, the host material should have high purity in order to prevent this.

6. *Chemically and physically stable.* The host material should be mechanically hard and stable and it should also posses high thermal stability and conductivity.

7. *Fabrication technology.* Finally, the host material should be easy enough to fabricate and doped with the current fabrication technology. Of course, the host material should also be cheap and the technology that provides the host material should be compatible with the integrated devices that use the amplifier.

In general, there are two types of materials that can be used as a host for the Er-ions: crystalline and amorphous. A crystalline host consists of well-defined crystal planes and atomic orientations whereas this kind of organized structure cannot be found in amorphous hosts. The behaviour of the Er-ions in both of these material types differ greatly with respect to each other. However, both material types offer their own advantages that depend on the application at issue.

Crystalline hosts offer very narrow absorption and emission spectra as well as high peak cross-sections because of the well-oriented crystal structure of the atoms. In crystalline hosts, very little to none defects and local variations can be found, leading to reduced phonon broadening and energy-band generation. Moreover, the crystalline structure also offers high thermal conductivity for electrons which enables

more stability [36]. There are two types of crystalline hosts that can be used: dielectrics and semiconductors. Dielectrics are transparent, offer high band-gap and low propagation losses. Semiconductors in turn have small band-gap and offer high refractive index contrast for tight confinement of light. Semiconductors can also be electrically pumped, thus, they allow the building of electro-optical devices. Nevertheless, crystalline hosts suffer major drawbacks when considering them as suitable host materials for the Er-ions in the amplifier devices. The absorption and emission spectra of the Er-doped crystalline hosts are usually too narrow and their fabrication is heavily limited due to lattice matching with the substrate [11].

Table 2: Different types of host materials for Erbium-ions. [11]

Host type	Material type	Examples	Advantages	Disadvantages
Amorphous	Glass	Silicate glass, Phosphate glass, Fluoride glass, Bismuthate glass, a-Al_2O_3	Wide bandwidth, isotropic, easy to fabricate, compatible	Low refractive index
	Polymer	PMMA, PPMA	Wide bandwidth, low cost, easy to fabricate	Thermally unstable, color centers
Crystalline	Dielectric	Y_2O_3, Lu_2O_3, $LiNbO_3$	High σ_{21} and σ_{12}, thermal stability	Narrow bandwidth, lattice-mathcing required
	Semi-conductor	GaAs, GaN, InP, ZnO, Si	High σ_{21} and σ_{12}, high index contrast, electro-optics, integration	Narrow bandwidth, low Er solubility, lattice-mathcing required

Contrary, amorphous hosts offer broad absorption and emission spectra because of both homogeneous and inhomogeneous broadening of the transitions. Although the peak cross sections of these spectra are somewhat smaller, the amplification can be realized over smooth and wide bandwidth, which is very important in the case of telecommunications. Amorphous hosts can also be divided into two main types: glasses and polymers. Polymers are organic materials that are cheap and easily fabricated. However, they are not thermally very stable and they exhibit so called color centers that create additional spectral lines [11]. Amorphous glasses, in contrast, tend to be excellent hosts because they are thermally very stable and also easily fabricated on various substrates [38]. Therefore, amorphous glasses, such as silicate glass, phosphate glass, fluoride glass and amorphous sapphire are attractive choices for the Er-ions. Yet, the low refractive index of glasses limit the index contrast in the waveguide devices, preventing large integration density of glass-based amplifier devices.

All in all, the advantages and disadvantages of all the suitable materials and material types are summarized in Table. 2.

3.4.2 Fabrication techniques

There are many fabrication methods that can be used to produce Er-doped materials, each with their own advantages and disadvantages. At least, the following fabrication methods have been used to produce erbium as dopant in suitable host materials: Atomic layer deposition [15], dip-coating [16], flame hydrolysis [17], high-vacuum chemical vapour deposition [18], plasma-enhanced chemical vapour deposition [19], pulsed laser deposition [20], reactive co-sputtering [21], RF-sputtering [22], sol-gel method [23], spin coating [24] and vapour phase deposition [25]. Some of these fabrication methods can be used to deposit the host material at the same time as the doping of the Er-ions is done. However, the doping technique of these methods differ from each other somewhat radically. In most of these techniques, the doping leads to non-uniform distribution of the Er-ions in the host material.

As was discussed previously in this chapter, the ETU-processes are important when the doping concentration becomes high in the amplifier. The probability for any ion-ion interaction process is proportional to $1/r^6$, where r is the distance between the neighboring ions [11]. In short devices, this brings major challenge in implementing the Er-ions into the host material because the dimensions of the device cannot be changed. Therefore, the only way to maximize the number of the Er-ions to realize high amplification, and hence, gain, is to increase the density of the Er-ions. Besides the distance between adjacent ions, the probability for the ETU-process to occur has also been found to depend on the homogeneity of the Er-ion profile [11]. Thus, the fabrication method must possess the ability to control the Er-ion profile in the host material to avoid the ion-ion interactions that lead to the energy-transfer up-conversion in the amplifier. Besides the control of the Er-ion profile inside the host material, it is very ideal if the fabrication technology could offer the production of the host material and the application to integrated devices as well. It turns out that ALD, which has been chosen as the fabrication method in this work can offer all of these techniques at the same time and in a single run. Therefore, ALD offers an unique way to fabricate Er-doped amplifier devices.

4 Atomic layer deposition

ALD is a chemical vapour phase deposition method that can produce thin films with excellent quality. It was first demonstrated by Suntola *et al.* as atomic layer epitaxy in 1977 in Finland [48]. Since then, ALD has gained much popularity as an alternative thin film deposition technique due to its unique deposition properties, such as high conformality, aspect ratio and non-uniformity. As the semiconductor industry has ever increasing demand for the miniaturization of components, new deposition techniques are needed in order to coat these nanometer-sized structures conformally with very high aspect ratio. ALD is the answer to this problem because no other thin film technique can approach the conformality achieved by ALD on high aspect structures [49].

4.1 Operation principle

The operation of ALD is based on the sequential use of a gas or vapor phase chemicals. As distinct from the other vapor phase techniques, in ALD, the source vapors are pulsed into the reactor alternately, one at a time [26]. This results in a unique self-limiting film growth mechanism with a number of advances as discussed in Section 4.3.

The basic operation cycle of ALD is divided into 4 main steps as shown in Fig. 12. In order to inititate the growth of the film, the first reactant is pulsed into the chamber under vacuum to react with the substrate surface for designated amount of time. The deposition temperature is typically $100^\circ\,\mathrm{C} - 300^\circ\,\mathrm{C}$ but can be as high as $500^\circ\,\mathrm{C}$ for some processes. When the exposure of the first reactant ends, a purge step follows. The purging is done using an inert gas, typically N_2 or Ar to remove both the reactant that did not react with the substrate surface and any other chemicals that was produced from the reaction. Then, the second reactant is pulsed into the chamber for designated amount of time to react with the substrate that already has one sublayer of the first chemical. The result is a molecular monolayer of the material that was chemically produced from the two reactants. Finally, another purge step follows to remove remaining chemicals and by-products. The deposition then continues to repeat this cycling procedure until appropriate film thickness is achieved. [48]

One cycle of ALD typically deposits no more than 1Å of the desired material. This depends, of course, on the precursors and the deposition parameters that are used during the process. The deposition rate is often expressed as (Å/cycle) and the deposition rates can vary from 0.10 Å/cycle with heavy and/or poorly reacting materials to approximately 2 Å/cycle with light and/or strongly reactive materials [50]. The most important parameters that determine the growth rate of the deposition inside an ALD reactor are shown in Fig. 13. In ALD, all these parameters have to be optimized for every material separately. When optimized, the growth rate of the deposition remains constant for every process cycle that occurs in the reaction chamber. The constant deposition rate is often observed in a specific temperature range, which is referred to as the ALD-window of the material. One should always

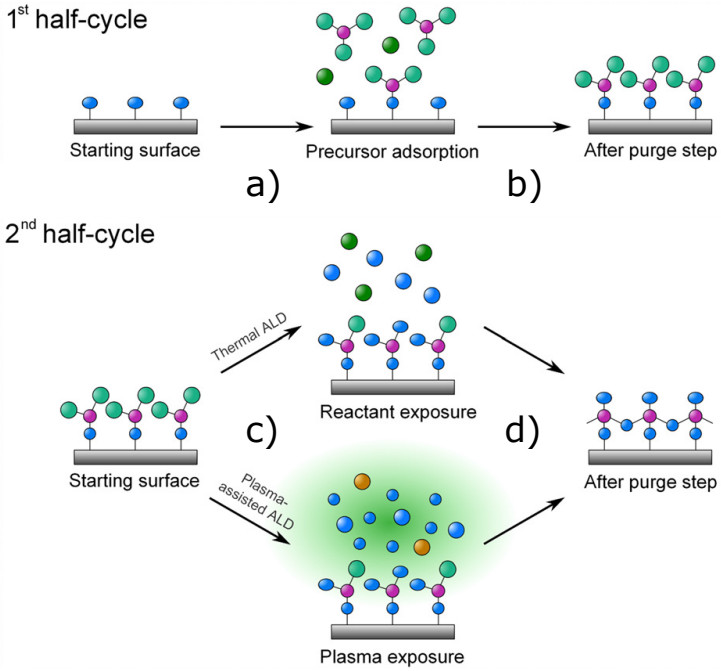

Figure 12: The operation principle of ALD. One deposition cycle consits of four main steps: a) pulsing of the first precursor; b) purge of the first precursor; c) pulsing of the second precursor and d) purge of the second precursor. [32]

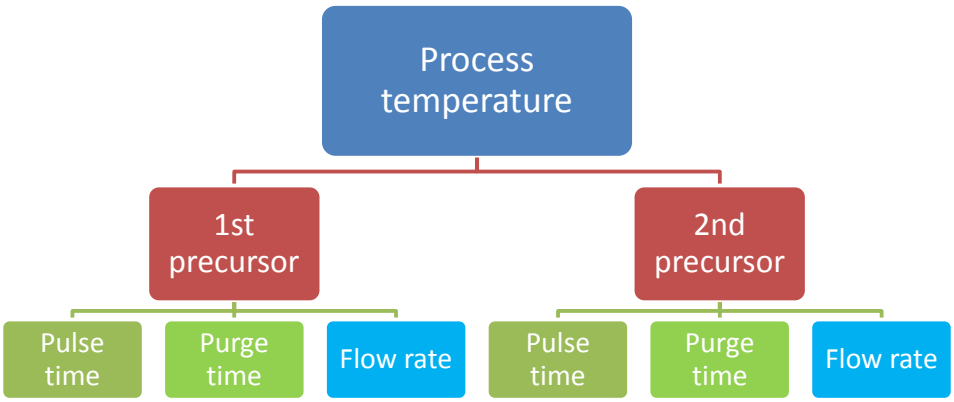

Figure 13: The most important ALD parameters that affect the growth rate of the deposited material.

choose the deposition temperature of the process inside this ALD-window; otherwise the growth of the material cannot be predicted and the deposition may not have the

properties that are unique for ALD.

The duration of one cycle in ALD can be calculated from the pulse and purge durations. If t_{pr1} and t_{pu1} are the pulse and purge times of the first precursor, respectively and t_{pr2} and t_{pu1} the pulse and purge times of the second precursor, respectively, the total time that it takes to complete one cycle is given by

$$\text{Duration of one cycle} = t_{pr1} + t_{pu1} + t_{pr2} + t_{pu2} \tag{6}$$

and the total process time is given by

$$\text{Process time} = \text{Number of cycles} \times \text{Duration of one cycle.} \tag{7}$$

4.2 Supported materials

The reactants that are pulsed into the ALD chamber are often referred to as precursors. The first precursor is typically a basic element like metal or semiconductor and the second precursor is a simple gas like oxygen, hydrogen or nitrogen. The precursor chemicals are usually molecules in some form which contain the materials that one wants to grow. For example, the growth of TiO_2 requires Ti and O_2 to create the end product. The precursors one usually uses are $TiCl_4$ and H_2O so the corresponding chemical process that occurs in the ALD reactor is [49]

$$TiCl_4 + 2H_2O \rightarrow TiO_2 + 4HCl. \tag{8}$$

In ALD, the growth of the material is based on the reactivity of the chemicals that are pulsed on the substrate. Under normal conditions, the chemical reactions cannot occur because the chemicals require some amount of energy to complete the reaction. Therefore, different types of operation modes of ALD has been developed to support this chemical reaction process in the deposition chamber. In traditional ALD, or thermally-driven ALD, one simply uses high enough temperature for the chemical process to occur. Most ALD-materials can be grown using thermally-driven ALD [50]. The above process for TiO_2 is an example of a thermal ALD process.

However, the thermal energy that one uses to produce the chemical reaction in the thermal ALD is not sufficient for all materials. For example, some metals, metal nitrides and metal oxides require larger amount of energy to complete the chemical reactions [49]. Fortunately, an alternative deposition technique have been developed to fabricate these weakly reacting materials: Plasma-enhanced ALD (PEALD) or Plasma ALD [51].

Plasma can be regarded as the fourth state of the matter. It occurs when a gas phase material is heated above specific temperature to ionize its molecules or atoms to produce a cloud of charged particles with very high energy [52]. The plasma itself is electrically neutral by average because it contains equal number of positively and negatively charged particles. Plasma ALD uses these high energy particles to assist the chemical reaction in the ALD chamber. Plasma can be generated by applying a very high electric field on a gas. The plasma gases that are typically used in PEALD are those generated by O_2, H_2 and N_2 or some combination of these [32].

PEALD has many advantages over thermal ALD. Firstly, the plasma process offers more freedom when choosing the deposition parameters because the chemical reaction can be easily produced. This includes the choosing of the precursors and deposition parameters [51]. Moreover, with PEALD, it is possible to deposit single-element ALD materials, such as metals or semiconductors which were not possible before the PEALD was invented [49]. For example, the fabrication of tantalium (Ta) can be produced with PEALD using hydrogen radicals as [49]

$$TaCl_5 + 5H\cdot \rightarrow Ta + 5HCl. \tag{9}$$

It has been reported that the materials deposited with the PEALD can have better material properties than those deposited with the thermal ALD. The material properties that are enhanced can be, for example, film density, impurity content or electronic properties [32]. Moreover, the plasma processes can be conducted at reduced substrate temperatures, because the thermal energy is replaced with the energy produced by the plasma. Furthermore, with PEALD, the growth rates are usually higher than those of thermal ALD because the plasma radicals generate higher density of reactive surface sites at the sample. The addition of plasma also

Table 3: Supported materials with PEALD. [32]

Plasma	H_2	O_2	N_2, N_2O or NH_3	H_2/N_2	O_2/N_2
Material	Ag, Al, Al_2O_3, Co, Cu, $GeSb_xTe_y$, HfN, NbN, Ni, Ta, TaC_xN_y, TaN_x, Ti, TiN_x, $TiAl_xN_y$, ZrN	Al_2O_3, $AlSi_xO_y$, Co_3O_4, $\mathbf{Er_2O_3}$, Ga_2O_3, HfO_2, $HfAl_xO_y$, $HfSi_xO_y$, La_2O_3, $LaHf_xO_y$, Pt, PtO_2, Ru, SiO_2, SnO_2, SrO, $SrTaO_6$, $SrTiO_3$, TaO_x, TiO_2, $TiSi_xN_y$, Y_2O_3, ZnO, ZrO_2, ZrN	Al_2O_3, AlN, $AlTi_xO_y$, Co, $CoSi_2$, HfN, HfO_2, Ir, NbN, Ni, $NiSi_2$, Ru, SiO_2, SiN_x, TaC_xN_y, TaN_x, TiN_x, TiO_2, $TiAl_xN_y$, WN_x, ZnO, ZrN	AlN, Co, HfN, NbN, Pd, Ru, TaN_x, TiN_x, $TiAl_xN_y$, $TiSi_xN_y$, ZrN	Al_2O_3, AlO_xN_y, $AlSi_xO_y$, HfO_2, HfO_xN_y, SiO_2, TiO_2, TiO_xN_y, ZrO_2

allows one to control the material composition because of the plasma radicals and additional parameters that can be controlled [50]. Table 3 lists all the materials that have been succesfully deposited with PEALD and the radical that has been used in the process [32].

4.3 Advantages and disadvantages

ALD in general offers a variety of advantages over other thin film deposition techniques. Firstly, because ALD produces films monolayer by monolayer, high-quality films with precise thickness, high aspect ratio and typically excellent conformality can be produced [53]. The layer-by-layer deposition of ALD allows the nanoscale engineering of the deposited film, which can be used to precisely design the composition of the ALD-grown materials. Because of this, it is also possible to grow multilayer films and nanolaminates with ALD [54]. Moreover, the growth of the material is not limited to flat surfaces: the material grows uniformly on every surface

of the sample that is placed in the reactor. This is a very important advantage when depositing thin films on complicated structures; there is no need to do additional lithography steps in order to fabricate desired structures. Thus, ALD has become very popular technique in silicon photonics where, for example, the top cladding of silicon slot waveguides can be fabricated very delicately [28, 55]. Contrary to other vapor phase techniques, such as chemical or physical vapor phase deposition, the moderate deposition temperature in also allows ALD to be used with integrated circuit structures to deposit high-k gate oxides [56].

Although ALD offers very impressive features, it also suffers from some drawbacks that limit its operation in general. Because of the layer-by-layer nature of the deposition and the purge processes used between each precursor pulsing, the deposition rate of ALD is very slow compared to other techniques. Most ALD materials require effective pathways for the chemical reactions to occur, thus, limiting the available precursors one can use [50]. Moreover, the precursors should be volatile enough to use them in gas phase at moderate temperatures [32]. Although the process support for materials is vast, one cannot grow some very important materials effectively with ALD. For example, most single-element metals, such as copper are very challenging to grow with ALD because the self-limiting growth cannot be reached easily with the precursors that are currently available for the processes [50].

4.4 Previous study on ALD-grown Er_2O_3

As was mentioned in Chapter 1, there are only few research groups that have studied the fabrication of Er_2O_3 with ALD. Therefore, the concept is still very young and requires further studies. Päiväsaari *et al.* have reported on the atomic-layer-deposited rare-earth oxides and their properties, especially in gate oxides. In [15], they fabricated thin Er_2O_3 films using tris(2,2,6,6-tetramethyl-3,5-heptanedionato) erbium ($Er(thd)_3$) and ozone as the precursors. They found that the growth rate of Er_2O_3 was 0.25 Å per cycle in the optimized deposition temperature window and precursor temperature of $250 - 375\,^{\circ}C$ and $130\,^{\circ}C$, respectively. In [56], Päiväsaari *et al.* deposited Er_2O_3 using $Er(CpMe)_3$ and water as the precursors in their ALD. They demonstrated that the growth rate of Er_2O_3 could be increased dramatically with this process, up to 1.5 Å/cycle with the deposition temperatures of $250\,^{\circ}C$ and $300\,^{\circ}C$.

Van *et al.* studied the growth of Er_2O_3 with radical-enhanced ALD using $Er(thd)_3$ and O-radicals. Van *et al.* was able to produce Er_2O_3 with the growth rate of 0.3 Å/cycle at the deposition temperature of $330\,^{\circ}C$ [30]. Xu *et al.* deposited Er_2O_3 with ALD using $Er(CpMe)_3$ and ozone as the precursors [29]. The growth rate of their films was 1.2 Å/cycle in the ALD temperature window of $170 - 330\,^{\circ}C$.

Blanquart *et al.* fabricated Er_2O_3 using three novel cyclopentadienyl precursors, $Er(PrCp)_3$, $Er(CpMe)_2$ and $Er(BuCp)_3$ with either ozone or water as the precursors in their depositions [31]. With $Er(MeCp)_2$, they reported the growth rates of 1.2 Å/cycle and 0.4 Å/cycle with water and ozone precursors, respectively. With Er(PrCp) precursor, Blanquart *et al.* reported the growth rates of 0.4 Å/cycle and 1.0 Å/cycle with ozone and water, respectively. In the last part, they obtained the

growth rates of 0.9 Å/cycle and 1.4 Å/cycle for the $Er(BuCp)_3$ precursor with ozone and water, respectively.

Table 4 summarizes the previous and on-going work on ALD-grown Er_2O_3. As can be seen, only Van *et al.* have studied ALD-grown Er_2O_3 using $Er(thd)_3$ and O_2 plasma as the precursor combination. However, in their case, the oxygen-radicals are produced from a completely different method as in this work.

Table 4: Previous and on-going work related to ALD-grown Er_2O_3.

Er precursor	2nd precursor	Temperature	Growth rate (Å/cycle)	Group	Year
$Er(thd)_3$	O_3	250 – 375 °C	0.25	Päiväsaari *et al.*	2004
$Er(CpMe)_3$	H_2O	250 – 300 °C	1.5		2005
$Er(thd)_3$	O_2	330 °C	0.3	Van *et al.*	2004
$Er(CpMe)_3$	O_3	170 – 330 °C	1.2	Xu *et al.*	2012
$Er(CpMe)_2$	H_2O	225 – 325 °C	1.2	Blanquart *et al.*	2014
$Er(CpMe)_2$	O_3	225 – 325 °C	0.4		2014
$Er(PrCp)_3$	H_2O	200 – 250 °C	1.0		2014
$Er(PrCp)_3$	O_3	200 – 250 °C	0.4		2014
$Er(BuCp)_3$	H_2O	275 – 325 °C	1.4		2014
$Er(BuCp)_3$	O_3	275 °C	0.9		2014
$Er(thd)_3$	**O_2**	**260-325°** C	0.21	**This work**	2014

5 Experimental tools

This chapter presents the fabrication and characterization tools related to this thesis. First, the ALD device that has been used to develop the process for Er_2O_3 is described. Then, the ellipsometer that is used to measure the thicknesses and refractive indices of the as-deposited samples is presented. Finally, the the optical setups that are used to measure the optical properties of the samples are expressed.

5.1 ALD-growth equipment

In this thesis, Picosun ALD R-200 advanced tool operating in the plasma-enhanced mode is used to fabricate Er_2O_3 [57]. The ALD system is presented in Fig. 14. The deposition of thin films takes place in the reaction (deposition) chamber. The

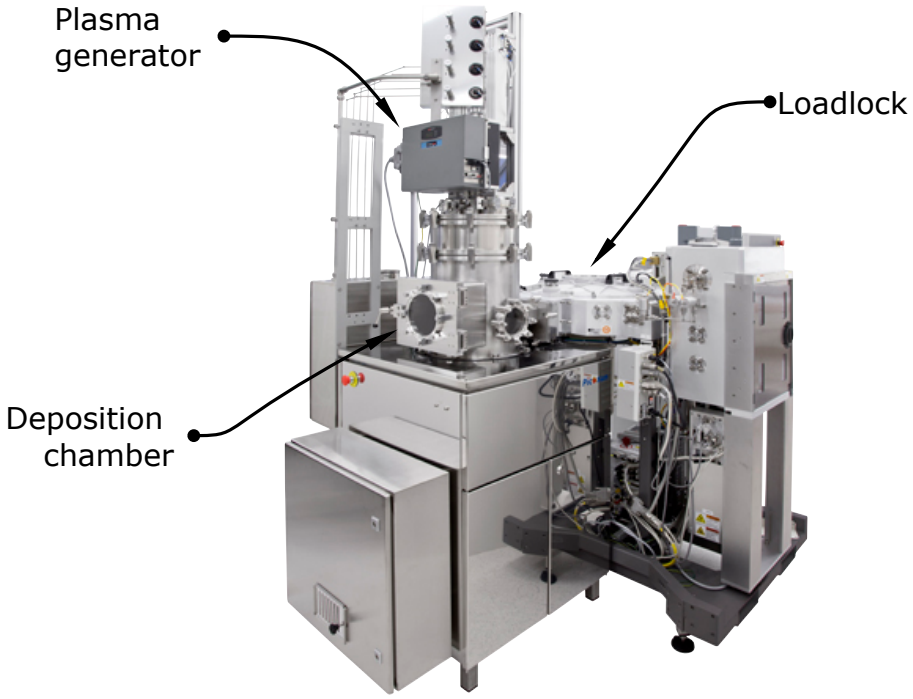

Figure 14: Picosun ALD R-200 advanced tool. [57]

ALD reactor has a dual chamber structure: the outer chamber is a vacuum chamber isolating the reactor from room air and the inner chamber is a reaction chamber that contains the substrate holder. All the precursor gas lines lead to the reaction chamber through a gas distributor. As there are separate input lines for all the precursor lines, no reactions of the chemicals can occur in the lines. The gas distributor spreads the precursors evenly to the complete area of the substrate, enabling high uniformity of the deposited layer.

The deposition chamber consists of six different precursor lines with additional four lines for the plasma-enhanced mode. The plasma gases one can use with the tool are NH_3, Ar_2/N_2, H_2/N_2 and O_2 and the highest usable plasma power is 2500 W.

The plasma in the R200 reactor is remotely controlled, that is, the plasma radicals are generated in the deposition chamber such that the generation of the radicals does not involve the substrate or the other precursors [32]. The locations of the precursor lines in the reaction chamber of the ALD tool are shown in Fig. 15. The locations of the precursor lines are important as the flow rates of the precursors have to be adjusted correctly for the growth to be located on the center of the wafer. The precursors that have been chosen for the fabrication of erbium oxide are tris(2,2,6,6-tetramethyl-3,5-heptanedionato) erbium and oxygen (O_2) plasma. The corresponding locations of these precursors are B for the Er-precursor and G for the plasma-precursor. All the precursor lines from A to E pulse from the sides of the chamber whereas the plasma pulses from above.

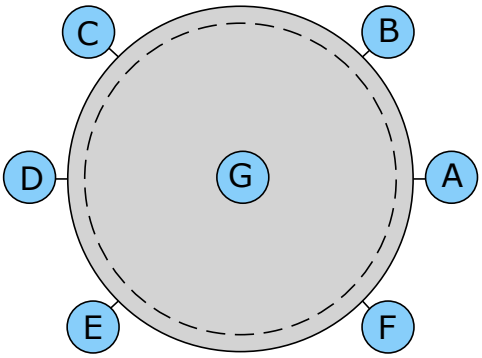

Figure 15: Locations of the precursor lines in the reaction chamber in Picosun ALD R-200 advanced tool.

The Picosun ALD R-200 advanced tool is used to optimize a model for the Er_2O_3 process by changing the ALD process parameters between each fabrication run. The studied ALD process parameters are: the source temperature of the Er-precursor, the flow rate of the Er-precursor, the pulse durations of both the Er-precursor and the oxygen plasma, the power of the plasma and finally, the deposition temperature.

5.2 Ellipsometry

Ellipsometry is an optical technique to characterize the dielectric properties of thin films with high precision. The properties can be, for example, the complex refractive index, the thickness profile, the doping profile, the surface roughness or the crystalline nature of the material under study. The operation principle of ellipsometry is to measure the change in the polarization state which occurs when the incident laser light has reflected from or transmitted into the sample. The change in the polarization is then compared to the model that the user has specified before the operation.

Figure 16 shows a typical schematic of an ellipsometer. The setup includes a laser source, a polariser, an analyzer and a detector. Unpolarised light is emitted

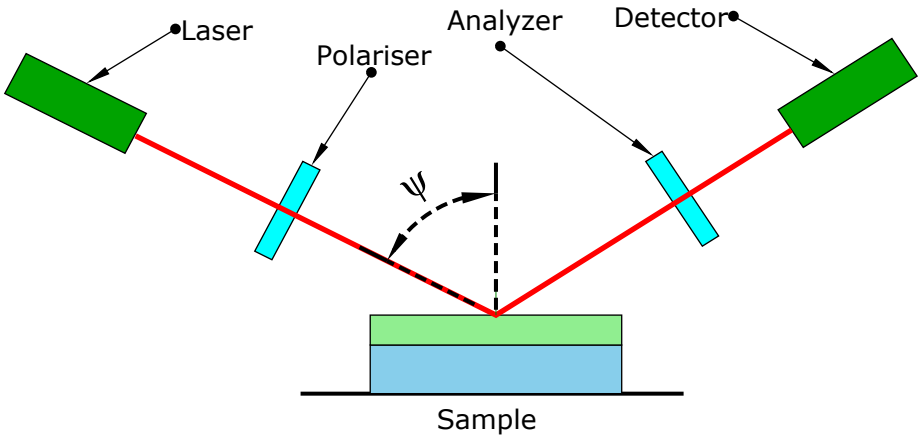

Figure 16: Schematic of an ellipsometry setup.

from the laser source into the polariser, which changes the polarisation state of the light from unpolarised to linearly polarised. When the light reaches the sample, a portion of the light is reflected and a portion of the light is transmitted into the sample. The reflected light can be divided into p- and s-polarised components of light, each having different Fresnel coefficients of reflectance r_p and r_s, respectively. Upon reflectance, a phase change of Δ develops between the s- and p-components of light. The detector measures this phase change with the help of the analyzer and the ellipsometry then calculates the complex reflectance ratio ρ as

$$\rho = \frac{r_p}{r_s} = \tan(\Psi)\, e^{i\Delta}, \tag{10}$$

where Ψ is the amplitude ratio of the reflected components [58]. The complex reflectance ratio is then compared to a model, from which the system calculates the properties of the sample, e.g. thickness of a film. The angle of reflectance ψ is chosen to be the Brewster angle of the light between the sample and air in order to maximize the sensitivity of the system [59].

In this thesis, Plasmos SD 2300 ellipsometer is used to measure the thickness profiles of the deposited films. It operates using He-Ne laser with the wavelength of 632.8 nm and the incidence angle range of $35 - 73°$. Plasmos SD 2300 ellipsometer calculates the average thickness t_{ave} of the deposition as the mean value of the measured points. The ellipsometer also gives the maximum t_{max} and minimum t_{min} values of the thicknesses. Once the average, maximum and minimum thickness of the sample under study are measured, the non-uniformity (n.u.) of the deposition can be calculated from

$$\text{n.u.} = \frac{t_{\text{max}} - t_{\text{min}}}{2t_{\text{ave}}}. \tag{11}$$

5.3 Photoluminescence setups

Photoluminescence (PL) or fluorescence is, by definition, the emission of light from any form of matter after the absorption of photons. The emission of light can occur

immediately after the excitation or after several nonradiative transition processes. The time between the absorption and emission of photons vary from femtoseconds to milliseconds, depending on the material under study [53]. PL can be used to investigate the excited state energies, their lifetimes or the emission spectrum of the material. It is often used to determine the bandgap energy of direct bandgap semiconductors [58].

In this thesis, two optical configurations are used to study the PL of the samples. At visible wavelengths, PL is studied using Quantamaster 40 (QM40) fluorescence spectrofluorometer [60]. The schematic of this setup is presented in Fig. 17. QM40 is

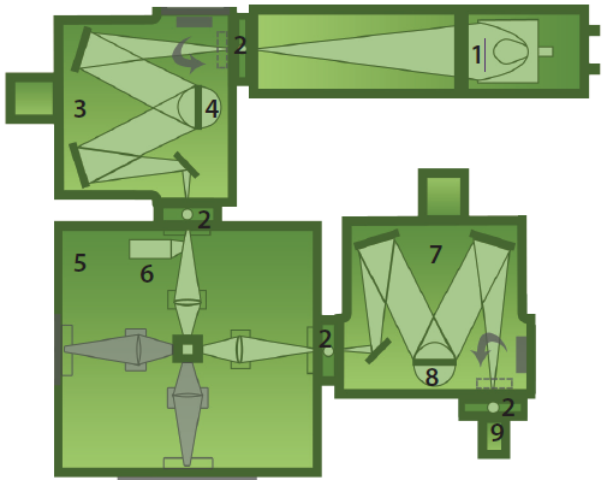

Figure 17: Schematic of the Quantamaster 40 fluorescence spectrofluorometer used in this work. The components and units in the setup are: 1: High intensity continuous Xe lamp, 2: Adjustable slits, 3: Excitation monochromator, 4: Excitation grating, 5: Sample compartment, 6: Excitation correction, 7: Emission monochromator, 8: Emission grating and 9: Detector. The sample to be studied is placed in the middle of the sample compartment. [60]

a very optimized system for the measurements of individual photons from fluorescent samples. Its signal-to-noise ratio is 10000:1 and detection limit of 460 attomolar of fluorescein solution can be reached. QM40 uses high intensity continuous Xe lamp as the excitation light source and the system contains several monochromators and gratings to separate the specific excitation and emission wavelengths of light.

QM40 can be used to measure both absorption and emission spectra of samples. However, the absorption measurement is done by measuring emission that results from the absorption process. Therefore, the system can only be used to study the locations of the absorption bands rather than the exact absorption of the material under study. This is because the emission at specific wavelength cannot be related to the absorption at another wavelength entirely.

QM40 has both excitation and emission corrections as all light sources emit light that is not of equal intensity across the output spectrum, which can lead to errors in the measurement of both excitation and emission spectrum. During an

experiment, part of the excitation beam is diverted into a reference diode detector prior reaching the sample. The excitation detector performs excitation correction in real time and provides the user a corrected output that is independent of the excitation source characteristics or any temporal fluctuation of the lamp intensity, thus ensuring excellent stability of the signal [61]. A similar phenomenon exists for emission data. The detector in the QM40 setup can be used to measure light at wavelength regime $\lambda = 185 - 820\,\text{nm}$.

In this thesis, QM40 spectrometer is used to measure both the absorption and emission spectra of the samples at visible and near-infrared wavelengths. The emission measurements are divided into two sections. In the first section, two excitation wavelengths, $\lambda_{\text{exc}} = 480\,\text{nm}$ and $\lambda_{\text{exc}} = 532\,\text{nm}$ are chosen to measure the PL properties of the samples. In the second section, two different wavelengths $\lambda_{\text{exc}} = 800\,\text{nm}$ and $\lambda_{\text{exc}} = 980\,\text{nm}$ are chosen to study the up-conversion properties of the samples.

As the QM40 fluorescence spectrometer cannot be used to measure the PL at near-infrared (NIR) wavelengths, a separate PL-setup is used for this purpose. Figure 18 shows this experimental setup. Frequency-doubled Nd:YAG laser (Verdi,

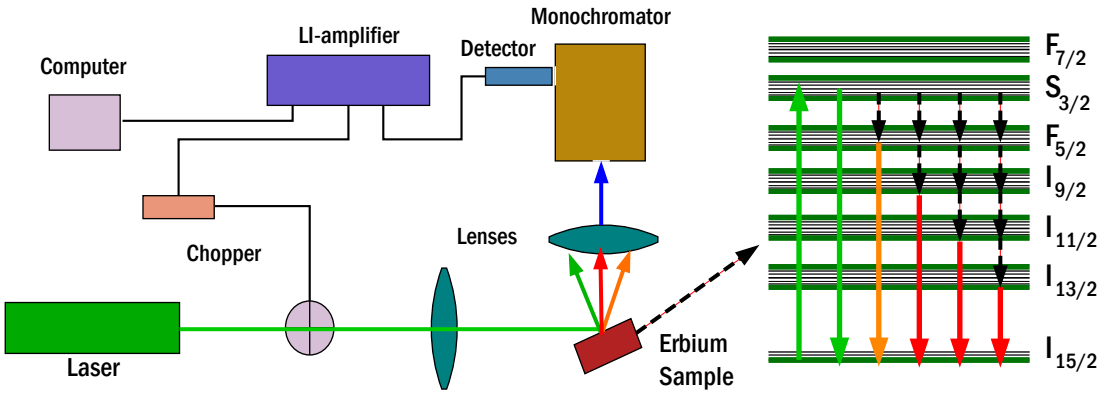

Figure 18: Schematic of the PL-setup used in this thesis to study the PL at NIR wavelengths.

Coherent inc.) is used as the excitation source to produce light with the wavelength of $\lambda = 532\,\text{nm}$. Continuous wave operation is used and the power levels from 1 W to 1.5 W are selected. The laser light is transmitted through a chopper operating at frequency $f = 330\,\text{Hz}$ and then directed onto the sample with very wide angle ($> 150°$). The sample is then excited and the radiation it emits is gathered with a lens. The emitted light is then directed into a monochromator, which passes only one wavelength component at a time to the detector. The voltage of the detector is measured as a function of the wavelength with a lock-in (LI) amplifier in order to increase the sensitivity of the system. The lock-in amplifier is connected to a computer which gives the data of the signal measured by the system.

In Er_2O_3, the pump wavelength of $\lambda = 532\,\text{nm}$ excites the ground state electrons into the $H_{11/2}$ band, where they can decay either radiatively or nonradiatively to any of the lower-lying energy bands $F_{5/2}$, $I_{9/2}$, $I_{11/2}$, $I_{13/2}$ or $I_{15/2}$. When the electrons decay to these lower-lying bands, they can again, decay radiatively or nonradiatively

to the lower bands. In this way, the possible PL-signals that can be observed are the wavelengths around the central wavelengths of the corresponding energy levels in the Er-ions, that is, 650 nm, 800 nm, 980 nm and 1530 nm or the ones generated via transitions to lower-lying energy bands other than ground state. However, there are also detrimental transitions present in the Er-ions as was discussed in Section 3.3.

6 ALD process development for Er_2O_3

In this chapter, the atomic-layer-deposited Er_2O_3 process development is presented thoroughly. The initial parameters for the first run were chosen based on the values Päiväsaari *et al.* used in [15]. Each run was performed on 6" p-type Si(100) wafer using a total of 1000 process cycles. After each process, the point-by-point thickness was measured with the ellipsometer and the average thickness and non-uniformity of the wafer were calculated from these values. The wafers were measured from 13 different points as shown in Fig. 19. The process development is divided into 5 subsections. In each subsection, the dependency of the ALD process parameters on the thickness and the non-uniformity of Er_2O_3 is studied one ALD parameter at a time. The influence of the erbium source temperature is studied first.

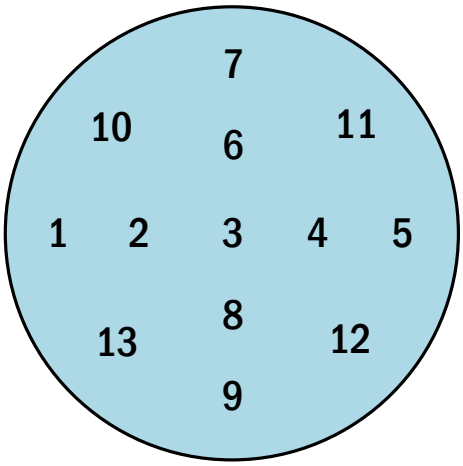

Figure 19: Locations of the measurement points for each wafer in the ellipsometer.

6.1 Erbium source temperature

The ALD parameters that were used in the first Er_2O_3 run are shown in Table 5. The first run was performed using the erbium source temperature of 140° C. With

Table 5: The ALD process parameters of the first Er_2O_3 run.

Dep./Source Temp.	$Er(thd)_3$ pulse / purge time	O_2 pulse / purge time	$Er(thd)_3$ flow rate	O_2 flow rate	Plasma power/time
325/140° C	2.5/6.0 s	13.0/2.0 s	150 sccm	150 sccm	2500 W/10 s

the initial values shown in Table 5, the average thickness and the non-uniformity of the first deposition was measured to be 136.85 Å and 38.18 %, respectively. The average thickness of 136.85 Å with 1000 cycles yields the deposition rate of approximately 0.137 Å/cycle, thus, it is likely that these results are far from what

could be expected from the process after optimization. After the first run, the temperature of the Er-precursor was increased in order to increase the growth rate and to decrease the non-uniformity of the deposition. The $Er(thd)_3$ solid precursor requires high enough temperature to produce a specific amount of vapor pressure for the chemical to reach out of the source bottle. The temperature of the source was first increased to 145° C and then to 150° C. The growth rate and the non-uniformity as a function of the temperature are shown in Fig. 20. In this figure, it

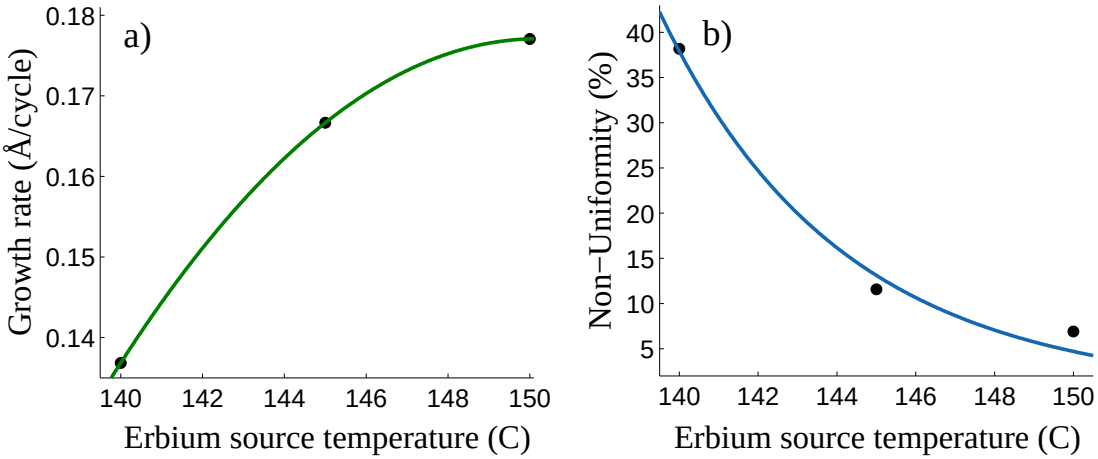

Figure 20: $Er(thd)_3$ source temperature vs. a) Er_2O_3 growth rate and b) Er_2O_3 non-uniformity. The unit of the x-axis is °C. The other growth parameters are: Deposition temperature: 325 °C, $Er(thd)_3$ flow rate: 150 sccm, $Er(thd)_3$ pulse/purge time: 2.5/6.0 s and O_2-plasma generation time/power: 10.0 s/2500 W.

is observed that the temperature of 140° C is indeed too low and yields poor growth rate and non-uniformity, whereas 150° C is high enough to reach the saturation of both the growth rate and the non-uniformity. However, Päiväsaari *et al.* showed that the $Er(thd)_3$-precursor starts to decompose around 150° C. Therefore, in order to ensure the best possible composition of the erbium chemical inside the reactor, 145° C was chosen as the temperature for the Er-precursor for the later runs.

6.2 Erbium precursor flow rate

To study the influence of the Er-precursor flow rate on the thickness and the non-uniformity of Er_2O_3, four runs were performed by using four different values for the flow rate: 150 sccm, 130 sccm, 110 sccm and 100 sccm. The thickness profiles of the process runs were studied in order to see where the growth of each deposition was located on the wafer. The first run in this series was performed using the same initial values as in the previous run, except that the erbium source temperature was increased to 145° C. The thickness profile of the first run is shown in Fig. 21. In Fig. 21, one can see that most of the growth is centered on the left side of the wafer. This indicates that the flow rate of either precursor is too low or too high. By examining

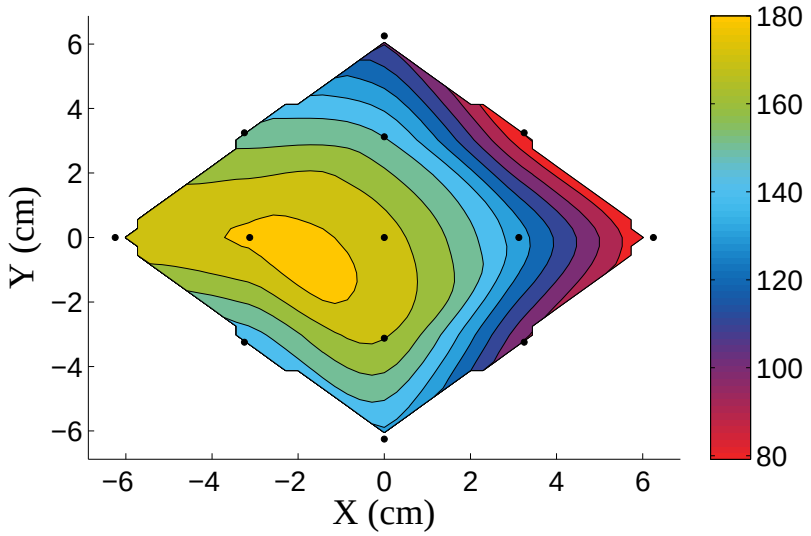

Figure 21: Er_2O_3 thickness profile when the $Er(thd)_3$ flow rate is set to 150 sccm. The unit of the color bar is Å. The other growth parameters are: deposition temperature: 325 °C, $Er(thd)_3$ source temperature: 145 °C, $Er(thd)_3$ pulse/purge time: 2.5/6.0 s and O_2-plasma generation time/power: 10.0 s/2500 W.

the locations of the precursor lines inside the deposition chamber of the Picosun ALD tool, it was observed that the Er-precursor is located on the north-east side of the chamber during the deposition. Thus, the flow rate of the Er-precursor must be too high. After the first run, the Er-precursor flow rate was decreased from 150 sccm to 130 sccm. The average thickness of 185.79 Å, which corresponds to the growth rate of 0.186 Å/cycle was observed and the non-uniformity remained approximately at the same value. The resulting thickness profile is shown in Fig. 22. By observing the thickness profile, one can clearly see that the center of the growth has slightly moved towards right of the wafer. Moreover, the vertical thickness of the deposition appears to be more uniform as compared to Fig. 21. Nevertheless, most of the growth still occurs on the left side of the wafer, thus, the flow rate requires more optimization.

In the third process run, the flow rate was decreased from 130 sccm to 110 sccm. The average thickness, the growth rate and the non-uniformity of the deposition was found to be 206.16 Å, 0.206 Å/cycle and 4.84 %, respectively. The thickness profile is shown in Fig. 23. As can be seen, the growth has shifted towards right and is now almost located at the center of the wafer. Motivated by this, a last process run for the Er-precursor flow rate was performed by reducing the flow rate from 110 sccm to 100 sccm. The average thickness, the growth rate and the non-uniformity of the deposition were found to be 209.26 Å, 0.209 Å/cycle and 4.12 %, respectively. The thickness profile is shown in Fig. 24. The thickness profile is now almost located at the center of the wafer and the uniformity appears to be excellent. As a result of the Er-precursor flow rate optimization, the growth was shifted to the center of the

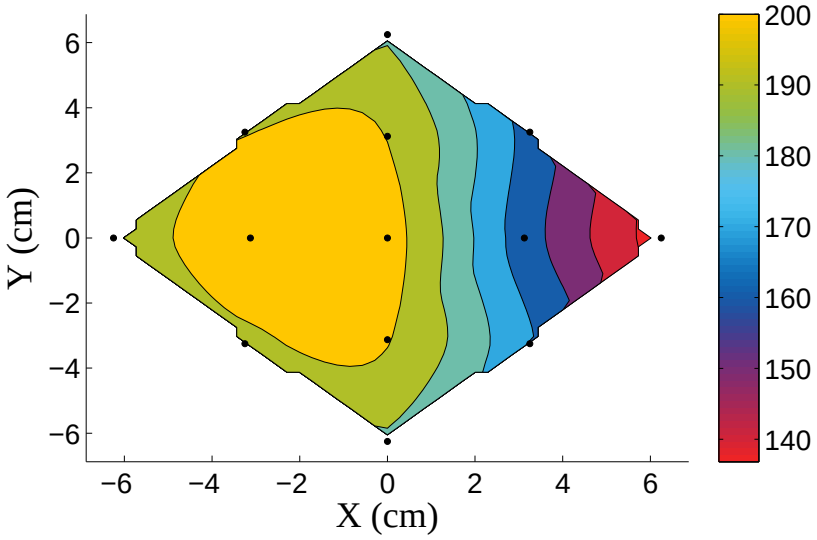

Figure 22: Er_2O_3 thickness profile when the $Er(thd)_3$ flow rate is set to 130 sccm. The unit of the color bar is Å. The other growth parameters are: deposition temperature: 325 °C, $Er(thd)_3$ source temperature: 145 °C, $Er(thd)_3$ pulse/purge time: 2.5/6.0 s and O_2-plasma generation time/power: 10.0 s/2500 W.

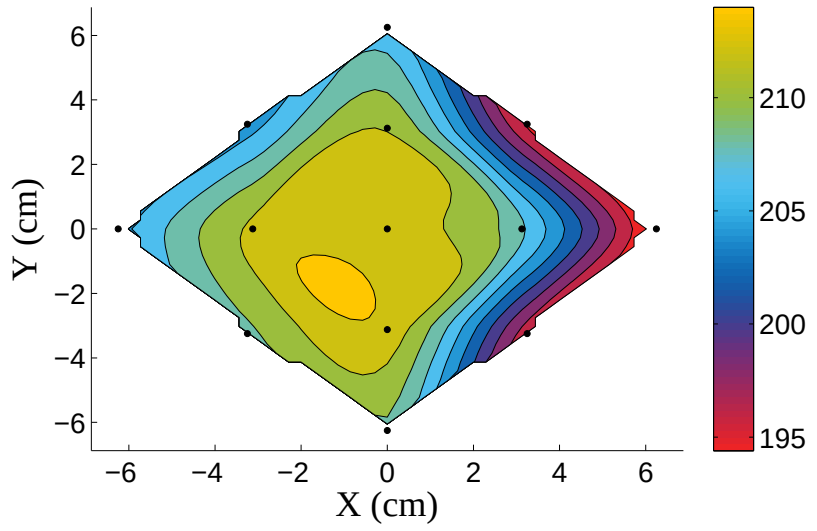

Figure 23: Er_2O_3 thickness profile when the $Er(thd)_3$ flow rate is set to 110 sccm. The unit of the color bar is Å. The other growth parameters are: deposition temperature: 325 °C, $Er(thd)_3$ source temperature: 145 °C, $Er(thd)_3$ pulse/purge time: 2.5/6.0 s and O_2-plasma generation time/power: 10.0 s/2500 W.

wafer and at the same time, the growth rate was increased above 0.20 Å/cycle and the non-uniformity was decreased to approximately 4 %.

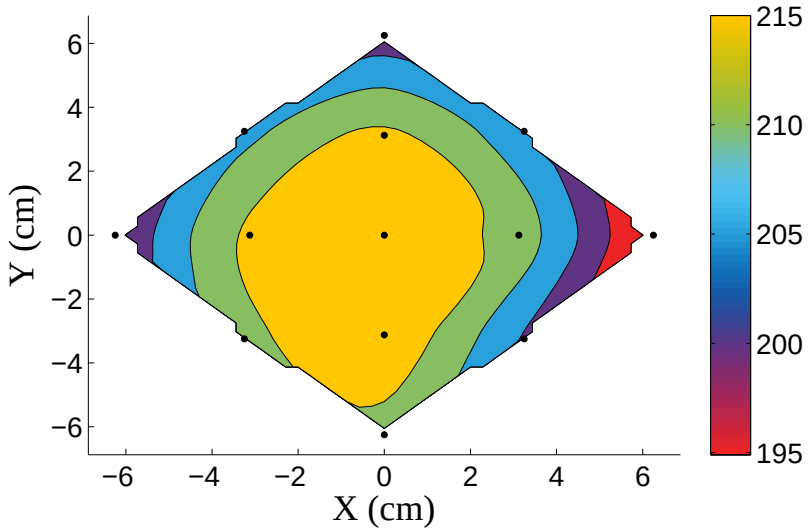

Figure 24: Er_2O_3 thickness profile when the $Er(thd)_3$ flow rate is set to 100 sccm. The unit of the color bar is Å. The other growth parameters are: deposition temperature: 325 °C, $Er(thd)_3$ source temperature: 145 °C, $Er(thd)_3$ pulse/purge time: 2.5/6.0 s and O_2-plasma generation time/power: 10.0 s/2500 W.

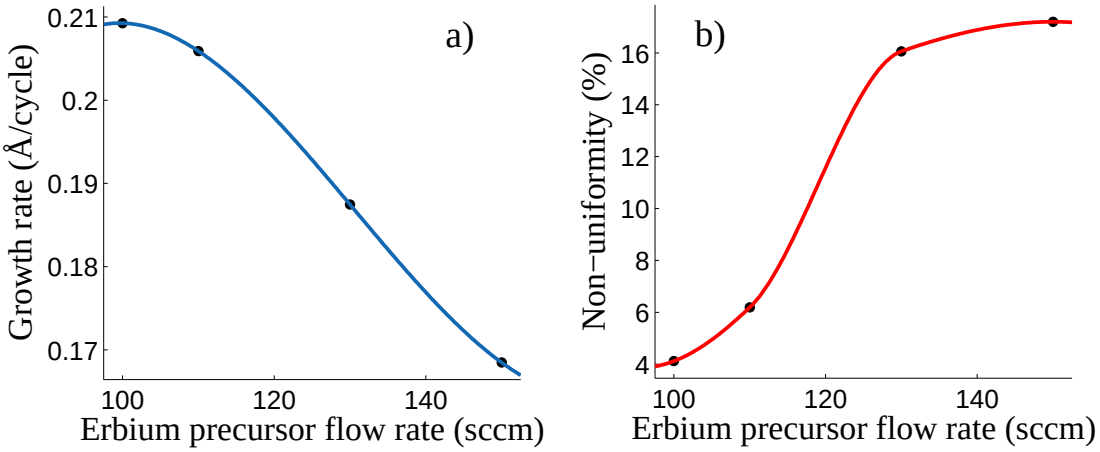

Figure 25: $Er(thd)_3$ flow rate vs. a) Er_2O_3 growth rate and b) Er_2O_3 non-uniformity. The other growth parameters are: deposition temperature: 325 °C, $Er(thd)_3$ source temperature: 145 °C, $Er(thd)_3$ pulse/purge time: 2.5/6.0 s and O_2-plasma generation time and power: 10.0 s/2500 W.

To summarize, the average thickness and the non-uniformity as a function of the $Er(thd)_3$ flow rate are shown in Fig. 25. It appears that both the non-uniformity and the growth rate have reached their saturation value. Thus, there was no need for further optimization and the process development was proceeded to optimize the pulse times of the precursors.

6.3 Precursor pulse times

The growth rate and the non-uniformity of the deposited Er_2O_3 was studied as a function of the precursor pulse times. First, the influence of the Er-precursor pulse duration was investigated. Five pulsing times were chosen: 1.0 s, 1.5 s, 2.0 s, 2.5 s and 3.0 s. Besides the Er-precursor pulse times, the other ALD process parameters that were used in the optimization process are shown in Table. 6. The growth rate

Table 6: The ALD process parameters for the optimization of the $Er(thd)_3$ pulse time. X varies from 1.0 s to 3.0 s.

Dep./Source Temp.	Er pulse / purge time	O_2 pulse / purge time	Er flow rate	O_2 flow rate	Plasma power/time
325/145° C	X/6.0 s	13.0/2.0 s	100 sccm	150 sccm	2500 W/10.0 s

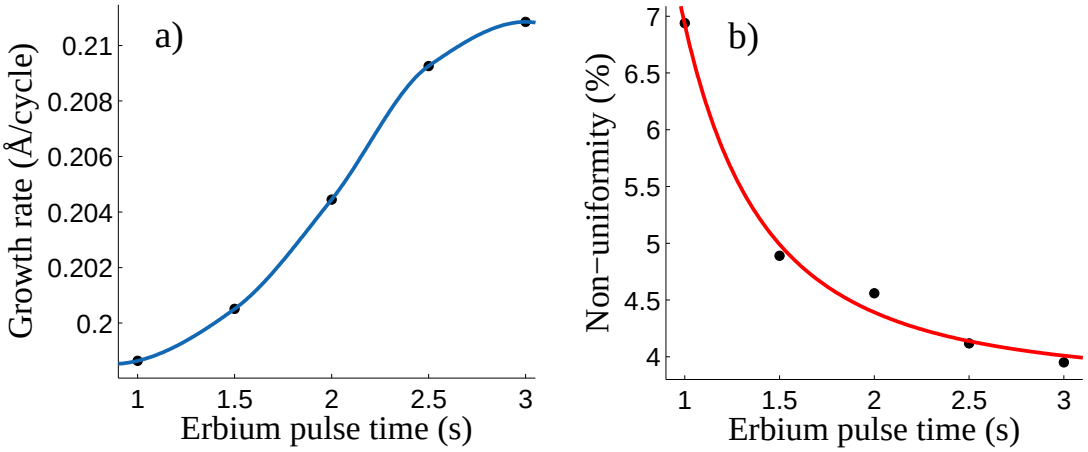

Figure 26: $Er(thd)_3$ pulse time vs. a) Er_2O_3 growth rate and b) Er_2O_3 non-uniformity. The other growth parameters are: deposition temperature: 325 °C, $Er(thd)_3$ source temperature: 145 °C, $Er(thd)_3$ flow rate: 100 sccm, $Er(thd)_3$ purge time: 6.0 s and O_2-plasma generation time and power: 10.0 s/2500 W.

vs. $Er(thd)_3$ pulse time is shown in Fig. 26a and the non-uniformity vs. $Er(thd)_3$ pulse time is shown in Fig. 26b. Again, it appears that both the non-uniformity as well as the growth have reached their saturation value. Therefore, pulse duration of 3.0 s was chosen as the best value.

After the Er-precursor pulse time optimization, the dependency of the O_2-plasma exposure time on the thickness and the non-uniformity of the process was studied. Again, five exposure times were chosen: 5.0 s, 8.0 s, 10.0 s, 15.0 s and 20.0 s. The Er-precursor pulse time was set to 2.5 s. The growth rate vs. O_2-plasma exposure time is shown in Fig. 27a whereas the non-uniformity vs. O_2-plasma exposure time is shown in Fig. 27b. In Fig. 27, it can be observed that the saturation of the non-uniformity can be reached with 20.0 s exposure time while the growth rate could be

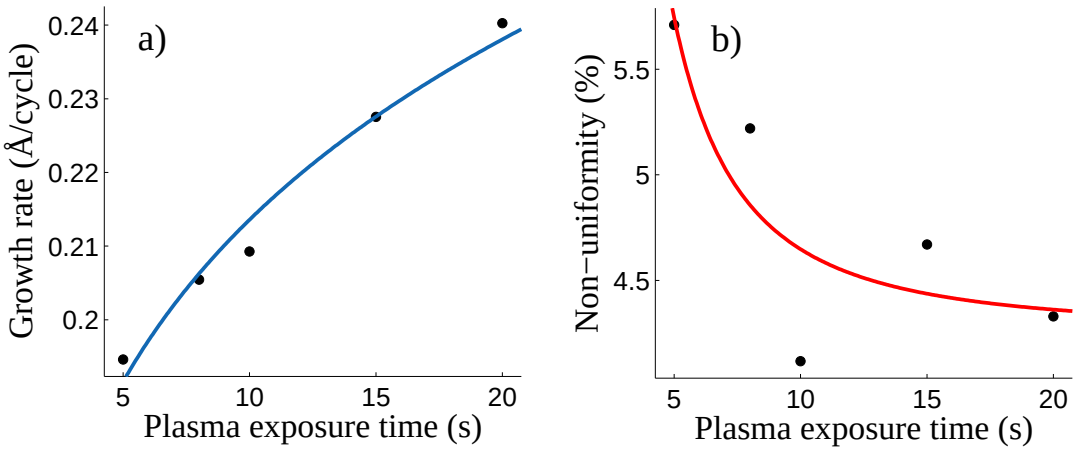

Figure 27: O_2-plasma exposure time vs. a) Er_2O_3 growth rate and b) Er_2O_3 non-uniformity. The other growth parameters are: deposition temperature: 325 °C, $Er(thd)_3$ source temperature: 145 °C, $Er(thd)_3$ flow rate: 100 sccm, $Er(thd)_3$ pulse/purge time: 2.5/6.0 s and O_2-plasma generation power: 2500 W.

made higher by increasing the plasma exposure time even further. Nevertheless, the growth rate was increased from approximately 0.21 Å/cycle to approximately 0.24 Å/cycle by increasing the plasma exposure time from 10.0 s to 20.0 s.

However, the tradeoff with higher growth rate is the dramatic increase in the process duration. For example, 1000 cycles of Er_2O_3 with plasma exposure time of 10.0 s takes approximately 6.5 hours whereas it takes 9.3 hours with 20.0 s exposure time. Thus, there is no need to use high duration plasma pulses because the same amount of film thickness could be produced by adding few more cycles to the process. Although this increases the consumption of the Er-precursor slightly, it saves time more than 2 hours per run. Therefore, exposure time of 10.0 s is chosen as a compromise because the process runs would be too long with the longer exposure times.

6.4 Plasma power

After the precursor pulse times were optimized, the dependency of the plasma generation power was studied. Three plasma generation power values were chosen: 1500 W, 2000 W, and 2500 W. 2500 W was the maximum power that could be utilized with the plasma generator of the ALD tool. The growth rate and the non-uniformity as a function of the plasma power are shown in Fig. 28. As can be observed in Fig. 28a., the growth rate reaches its saturation value at approximately 2000 W. However, the non-uniformity can still be lowered by increasing the plasma power, as can be seen in Fig. 28b. Because 2500 W is the highest value that can be used, it is chosen as the best value due to the highest growth rate and the lowest non-uniformity.

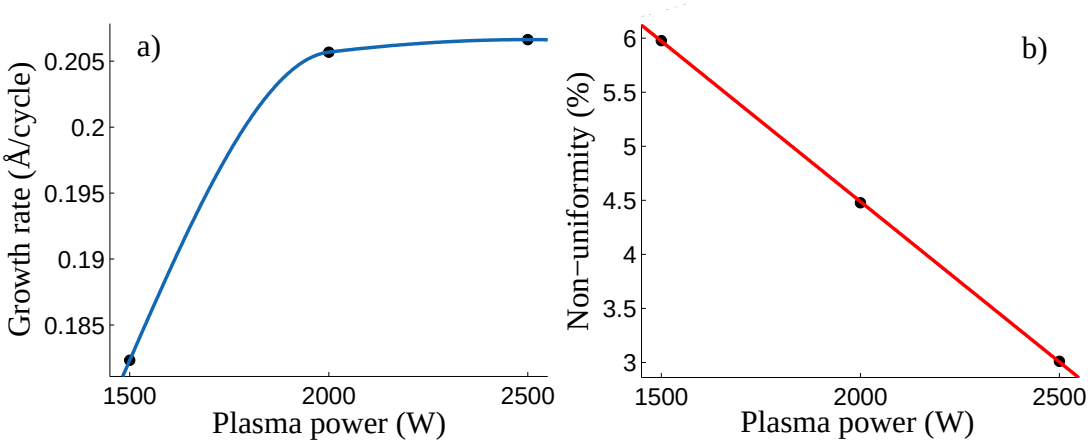

Figure 28: O_2-plasma generation power vs. a) Er_2O_3 growth rate and b) Er_2O_3 non-uniformity. The other growth parameters are: deposition temperature: 325 °C, $Er(thd)_3$ source temperature: 145 °C, $Er(thd)_3$ flow rate: 100 sccm, $Er(thd)_3$ pulse/purge time: 2.5/6.0 s and O_2-plasma generation time: 10.0 s.

6.5 Deposition temperature

Once the Er-precursor temperature, flow rate and pulse time as well as the O_2-plasma exposure time and generation power were optimized, the deposition temperature was studied last. The deposition temperature was varied between 250° C and 325° C and the growth rate of Er_2O_3 was studied for each temperature. Fig. 29 shows the

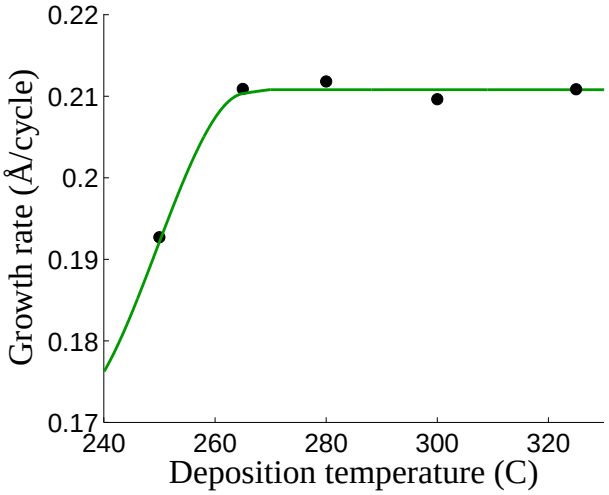

Figure 29: Deposition temperature vs. Er_2O_3 growth rate. The unit of the x-axis is °C. The other growth parameters are: $Er(thd)_3$ source temperature: 145 °C, $Er(thd)_3$ flow rate: 100 sccm, $Er(thd)_3$ pulse/purge time: 2.5/6.0 s and O_2-plasma generation time/power: 10.0 s/2500 W.

results. In this figure, a constant growth rate is obtained when the temperature reaches 260° C and the growth rate stays constant up to the deposition temperature

of 325° C. Thus, the ALD-window of the process is 250° C – 325° C. It is possible that this window extends to even higher temperatures, as was the case in the study by Päiväsaari *et al.* [15].

6.6 The optimized process

When the process optimization was completed, the process was tested by setting all the ALD-parameters to their optimal values. Figure 30 shows the Er_2O_3 thickness profile of this deposition. The growth rate and non-uniformity of this deposition

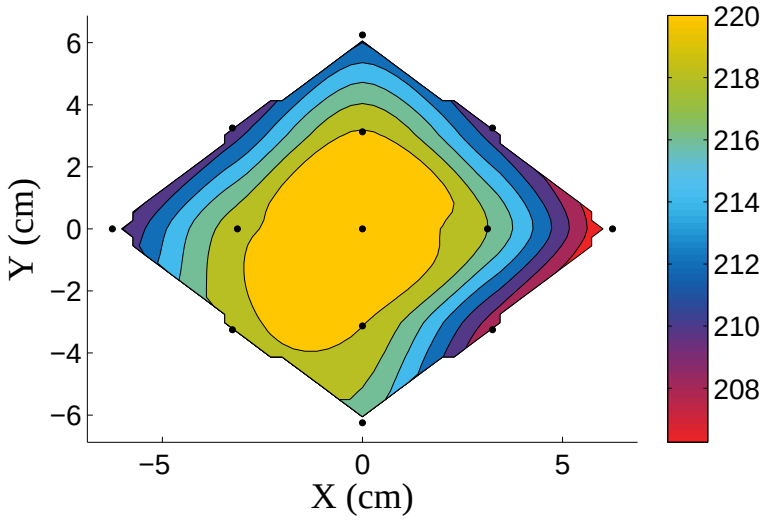

Figure 30: Er_2O_3 thickness profile after the optimization of the process. Average thickness: 214.53 Å and non-uniformity: 3.55%. The unit of the color bar is Å. The process parameters that were used in the deposition are shown in Table 11.

was calculated to be 0.215 Å/cycle and 3.55 %, respectively. The optimized ALD-parameters are listed in Table 11.

Table 7: The ALD parameters of the optimized Er_2O_3 process.

Dep./Source Temp.	Er pulse / purge time	O_2 pulse / purge time	Er flow rate	O_2 flow rate	Plasma power/time
325/145° C	3.0/6.0 s	13.0/2.0 s	100 sccm	∼ 150 sccm	2500 W/10.0 s

In order to verify that the process development was successful, the deposition rate of the optimized process should remain constant after each cycle. This was studied by performing three more process runs: one with 250 cycles, second with 500 cycles and third with 750 cycles. If the deposition rate remains constant after each cycle, it indicates that the thickness of the film is a linear function of the number of cycles. The film thickness as a function of the number of process cycles is

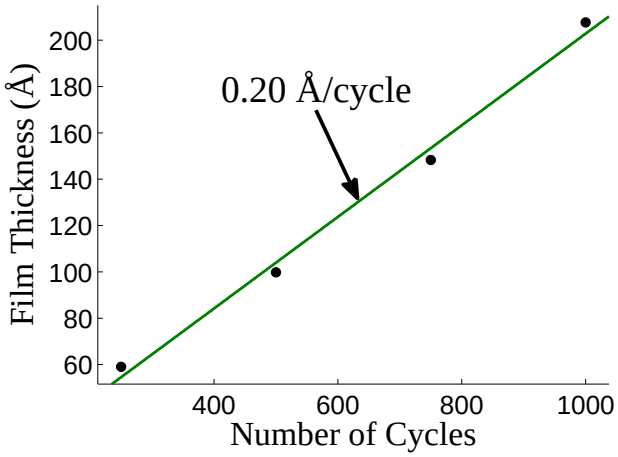

Figure 31: Number of process cycles vs. Er_2O_3 film thickness after optimization. The deposition rate is constant.

shown in Fig. 31 As can be seen, the film thickness follows the linear relation with the amount of cycles performed. The slope of the plot gives the deposition rate, which has been calculated to be approximately 0.20 Å/cycle.

In conclusion, this chapter provided a well-working ALD-process for the fabrication of Er_2O_3 using $Er(thd)_3$ and O_2-plasma as the precursors of the deposition. To my knowledge, this is the second time Er_2O_3 has been fabricated using ALD with O_2-plasma as the oxygen source. However, the generation of the oxygen radicals that react with the Er-precursor is completely different than the study provided by Van *et al.*, who used radically-enhanced ALD in their work. In the case of Van *et al.* the O-radicals (O, O^*, O^+, O^-, O_2, O_2^+ and O_2^*) are generated before reaching the deposition chamber, whereas in this work, the O-radicals are generated in the deposition chamber during the process. In their case, the generation of the radicals takes up to 10 minutes, whereas in this work, the generation time is only 10 seconds. Moreover, Van *et al.* only studied the surface kinetics of the reaction and did not provide any ALD-related information on their process. Therefore, Table 4 can be filled with new information related to the deposition of Er_2O_3 with ALD: the combination of $Er(thd)_3$ and O_2-plasma yields a constant growth rate of 0.21 Å/cycle in a temperature window of 260-325° C.

The growth rate and the deposition temperature are somewhat in a good agreement with Päiväsaari *et al.* whose deposition of Er_2O_3 yielded the growth rate of 0.25 Å/cycle in the temperature range of 250-375° C with the same Er-precursor but with ozone as the oxygen source [15]. The reason for the lower growth rate obtained in this work is most likely caused by the difference in the oxygen source as erbium requires O_3 to complete the reaction into Er_2O_3. In this work, the O_3 is provided by the plasma reaction of O_2 into O_3, thus, complicating the chemical reaction slightly. However, it is also possible that the difference is caused by the use of completely distinctive ALD-reactor in this work. Although it was shown that a deposition rate of 0.24 Å/cycle was reached with high plasma exposure time, the refractive index

of Er_2O_3 provided by this process cannot be referred to the literature value ≈ 1.9 [62]. As Päiväsaari *et al.* did not provide the refractive index of their Er_2O_3 films, it is impossible to confirm what causes the difference in the growth rates between this and their work.

The purge time or the flow rate of the O_2-plasma precursor were not studied in this process development, because the influence of the plasma purge time does not give any new information related to the process and the flow rate of the plasma cannot be controlled with the process software.

7 Optical characterization of Er_2O_3

Once the fabrication process was optimized for Er_2O_3, two more samples were fabricated in order to study the optical behaviour of Er-ions in different environments. The first sample was fabricated in the following way: the number of Er_2O_3 cycles was kept constant but in addition, 2 cycles of Al_2O_3 were added between each Er_2O_3 cycle. The second sample was fabricated in the same way but with 3 cycles of Al_2O_3 between each Er_2O_3 cycle. The fabrication process is shown in Fig. 32. By adding x amounts of Al_2O_3-layers between each Er_2O_3 layer, the Er-ions are doped to the Al_2O_3 and the average distance between the Er^{3+}-ions becomes larger in the vertical direction. Al_2O_3 has been chosen as the host material for the Er-ions because of its excellent properties as a host material, as was discussed in Section 3.4. The atomic-layer-deposited Al_2O_3 assumes an amorphous form. The deposition parameters for Al_2O_3 are shown in Table 8.

Table 8: the ALD parameters of the Al_2O_3 process.

Dep. Temp.	TMA pulse / purge time	O_2 pulse / purge time	TMA flow rate	O_2 flow rate	Plasma power/time
325° C	0.2/5.0 s	13.0/2.0 s	140 sccm	150 sccm	2500 W/10.0 s

Once the samples were fabricated, their average thicknesses and refractive indices were measured with ellipsometer. Each sample was given its own name for clarity. The names and the measured parameters are shown in Table 9. After

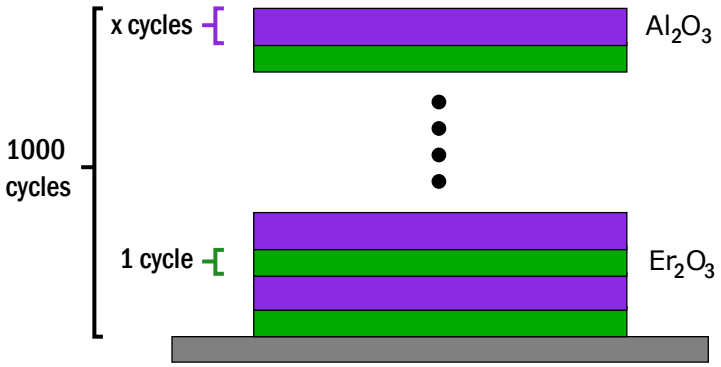

Figure 32: Fabrication process of the Er_2O_3-Al_2O_3 nanolaminates.

the fabrication, the absorption and emission spectra of the samples were studied using the QM40 fluorescence spectrometer and the PL setup that were presented in Chapter 5. QM40 was used to measure the absorption and emission spectra at wavelength range $480 - 900$ nm, whereas the PL-setup was used to measure PL at near infra-red wavelengths (> 900 nm).

Table 9: The experimentals details of each sample.

Sample	Al_2O_3-cycles	Er_2O_3-cycles	Process-cycles	L (nm)	n	n.u. (%)
Sample 1	0	1	1000	20	1.885	3.55
Sample 2	2	1	1000	163	1.668	3.11
Sample 3	3	1	1000	270	1.640	2.16

7.1 Absorption

In order to be able to study the PL of the samples, it is mandatory to know where the energy bands of the samples are located. The locations of the energy bands were studied by measuring the absorption spectrum of each sample. As was noted in Section 5.3, the principle of the absorption measurement with QM40 is to measure the emission that results from the absorption process. Therefore, no absolute values for the absorption of the samples can be given with this method. Moreover, the relative strengths of the absorption peaks in the absorption spectra cannot be compared between the samples. However, the method is still reliable to study the locations of the energy bands in the samples.

The absorption measurements were done as follows: First, the absorption was studied in the wavelength range $460 - 620$ nm by measuring the emission at $\lambda_{\text{em}} = 800$ nm. After this, the absorption was studied in the wavelength range $780 - 900$ nm by measuring the emission at $\lambda_{\text{em}} = 532$ nm. Finally, the absorption was studied in the wavelength range $900 - 1000$ nm by measuring the emission at $\lambda_{\text{em}} = 650$ nm. Fig. 33 presents the results from these measurements. In this figure, one can distinguish most of the transitions that are typical to the Er^{3+}-ions, although the peaks are not located at exactly the same wavelengths as in a standard absorption spectrum of Er^{3+}. This is because the composition of the Er-material and the environment of the Er^{3+}-ions are completely different than those of Er-ions that are usually doped into other glass-based materials, such as silica [9, 11, 43, 63, 64].

Table 10 lists the locations of the absorption peaks with the corresponding band-to-band transitions. The energy states are also labeled with band numbers, where, for example, 1 is related to the first excited state, 2 to the second excited state and so on. With these notations, the transition between bands 1 and 2 can be expressed as $1 \rightarrow 2$. The results show that the locations of the bands 2, 3 and 5 are in a good agreement with the ones reported in Er-doped Al_2O_3-samples [13, 14]. However, the location of the band 4 occurs at around 600 nm, whereas it is found at 650 nm in other glass- or Al_2O_3-based samples [44, 65]. Moreover, this transition cannot be found in the pure Er_2O_3 sample but is found in the both Er_2O_3-Al_2O_3 samples. There are two possible reasons for this: either the transition has shifted radically or it is somehow related to the presence of Al_2O_3. It is most likely that the latter of these is true as Al_2O_3 has absorption peak at exactly $\lambda = 600$ nm. Absorption at $\lambda = 600$ nm was also found in Er-doped Al_2O_3-samples in [14] but they stated that the origin of this peak was most likely caused by noise in their system. It

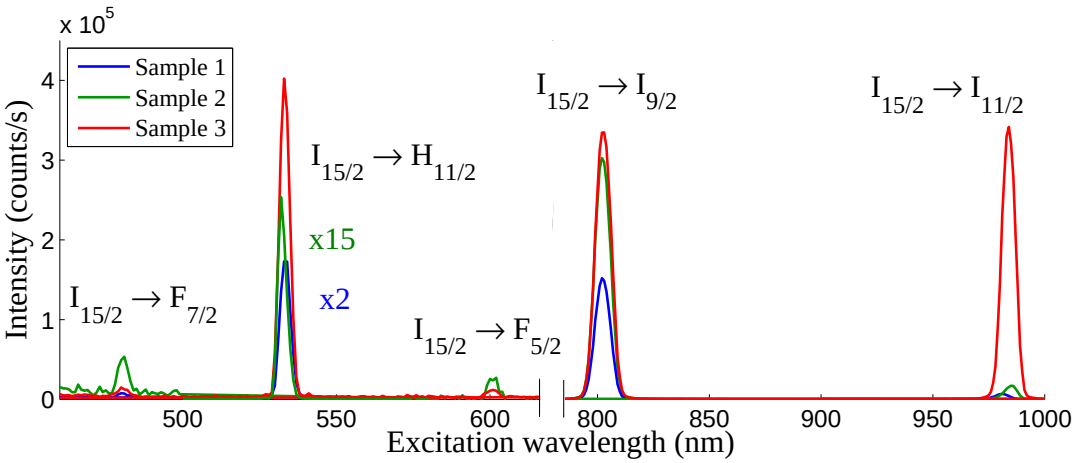

Figure 33: Absorption spectra of the samples in the wavelength range $\lambda = 460 - 1000\,\text{nm}$. The peaks of the spectra show the corresponding band-to-band transitions. The intensity of the peaks may not be related between wavelength ranges $\lambda_{\text{exc}} = 460 - 620\,\text{nm}$, $\lambda_{\text{exc}} = 780 - 900\,\text{nm}$ and $\lambda_{\text{exc}} = 900 - 1000\,\text{nm}$ because they are from different measurements. The peaks at 532 nm are reduced by a factor of 15 for the Sample 2 and by a factor of 2 for the Sample 1. The absorption spectrum of the first excited state could not be measured due to poor sensitivity of the detector at NIR wavelengths.

Table 10: Wavelengths of the absorption peaks of each sample with the corresponding band-to-band transitions and band numbers. The color of the peak wavelength is related to the sample as in Fig. 33. The absorption peaks that occur at wavelengths of 602 and 601 nm in Samples 2 and 3 cannot be related to the band-to-band transition $^4I_{15/2} \rightarrow {}^4F_{5/2}$ for sure.

Band number	Transition	Peak wavelengths
6	$^4I_{15/2} \rightarrow {}^4F_{7/2}$	480 nm, 481 nm, 480 nm
5	$^4I_{15/2} \rightarrow {}^2H_{11/2}$	533 nm, 532 nm, 533 nm
4	$^4I_{15/2} \rightarrow {}^4F_{5/2}$	-, 602 nm, 601 nm
3	$^4I_{15/2} \rightarrow {}^4I_{9/2}$	802 nm, 802 nm, 803 nm
2	$^4I_{15/2} \rightarrow {}^4I_{11/2}$	981 nm, 985 nm, 984 nm

is not a coincidence that this has occured again here. Although this peak would normally be much wider in general, the measurement has been made as emission at $\lambda_{\text{em}} = 800\,\text{nm}$ which could explain the shape of the transition. However, if this is the case, then the excitation at 600 nm could occur in the following: first, the photons with the wavelength around 600 nm are absorbed by Al_2O_3. The Al_2O_3 then transfers this energy to the Er-ions, which then emit the energy as light that has the emission wavelength of $\lambda_{\text{em}} = 800\,\text{nm}$.

Furthermore, the results also show that the location of the band 6 has blue-

shifted slightly. The band 6 is found at around 480 nm, whereas it is found near 490 nm in, for example, Er-doped silica [9]. Strongest signal is obtained in the Sample 2 at visible wavelengths and in the Sample 3 at NIR wavelengths. Moreover, the shapes of the peaks are found to follow Gaussian lineshape, which indicates that the transitions are inhomogeneously broadened. The peaks are also very narrow, which is a well-known charasteristic of the lanthanides. Bandwidths (FWHM) of $\Delta\lambda_{\text{exc}} = 4-5\,\text{nm}$ and $\Delta\lambda_{\text{exc}} = 8-9\,\text{nm}$ are observed at visible and NIR wavelengths, respectively.

7.2 Photoluminescence

Once the locations of the energy bands were discovered, two excitation wavelengths were chosen to study the PL of the samples: $\lambda_{\text{exc}} = 480\,\text{nm}$ and $\lambda_{\text{exc}} = 532\,\text{nm}$. These excitations correspond to the band-to-band transitions of $0 \rightarrow 6$ and $0 \rightarrow 5$ in the Er-ions, respectively. The emission measurements were divided into three parts: first, the fluorescence spectrometer was used to measure the PL at visible wavelengths with the excitation wavelength of $\lambda_{\text{exc}} = 480\,\text{nm}$. Then, the measurements were repeated by changing the excitation wavelength to $\lambda_{\text{exc}} = 532\,\text{nm}$. After these measurements, the PL was studied at NIR-wavelengths with the PL-setup using the excitation wavelength of $\lambda_{\text{exc}} = 532\,\text{nm}$.

7.2.1 Excitation at $\lambda = 480\,\text{nm}$

Fig. 34a shows the PL spectra of the samples at $500-820\,\text{nm}$ with the excitation wavelength of $\lambda_{\text{exc}} = 480\,\text{nm}$. The same spectra are shown in Fig. 34b in a smaller wavelength range in order to see the shapes of the spectra more clearly. In this

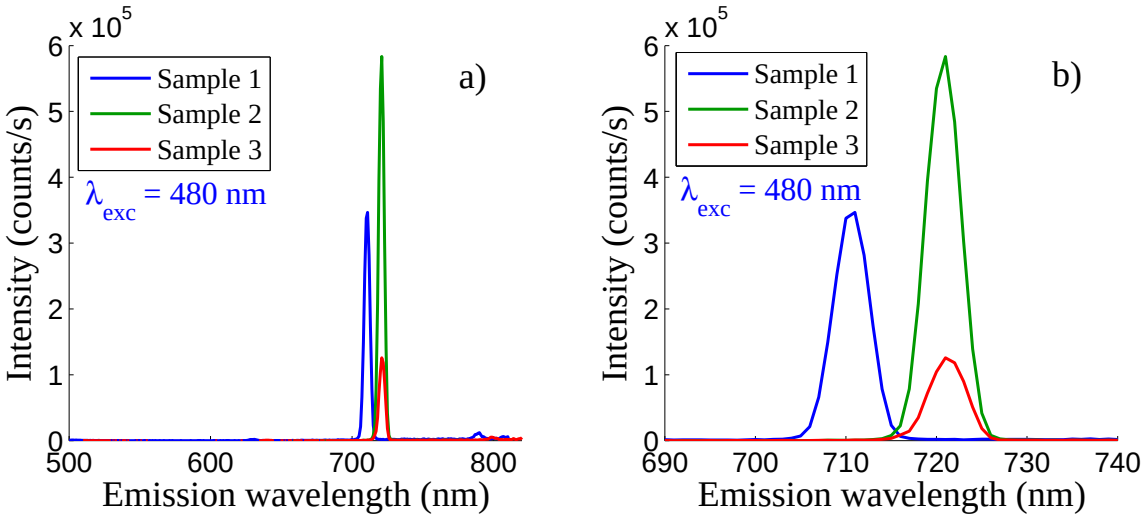

Figure 34: PL spectra of the samples at a) $500-820\,\text{nm}$ and b) $690-740\,\text{nm}$ with $\lambda_{\text{exc}} = 480\,\text{nm}$.

figure, transitions occur at $\lambda_{\text{exc}} = 711\,\text{nm}$ in the Sample 1 and at $\lambda_{\text{exc}} = 721\,\text{nm}$ in the Samples 2 and 3. Thus, the transition in the Sample 1 has 10 nm shorter peak

wavelength as in the Samples 2 and 3. This change is most likely caused by the difference in the host material of the Er-ions between the Sample 1 and the Samples 2 and 3. Nevertheless, in both cases, this wavelength can be related to the band-to-band transition $6 \rightarrow 1$, that is, the energy is emitted immediately from the band 6 into the band 1 where the remaining energy of the electrons correspond to the transition $1 \rightarrow 0$. Therefore, the presence of the band 1 that could not be measured in the absorption measurements can be confirmed by these results. Moreover, the transition is strongest in the Sample 2 and weakest in the Sample 3. In Fig. 34, one can also distinguish a small signal near 790 nm in the Sample 1 and at 800 nm in the Sample 3. These transitions can be related to the transition $3 \rightarrow 0$ in the Er-ions.

The results in this subsections are in a good agreement with Kasuya *et al.* who studied visible PL from an erbium-oxide overlayer on silicon [66] as they reported emission at the same wavelength but with the excitation wavelength of $\lambda_{\text{exc}} = 455\,\text{nm}$. The only difference is that their excitation wavelength excites the electrons from the band 0 to the band 7 ($F_{5/2}$), whereas the electrons are excited to the band 6 ($F_{7/2}$) in these measurements. Thus, to sum up, the energy from the excitation wavelength of $\lambda_{\text{exc}} = 480\,\text{nm}$ is released either immediately from the band 6 into the band 1 as photons with wavelengths $\lambda_{\text{em}} = 711\,\text{nm}$ (Sample 1), $\lambda_{\text{em}} = 721\,\text{nm}$ (Samples 2 and 3) or after many nonradiative transitions from the band 6 into the band 3 and then to the ground state as photons with $\lambda_{\text{em}} = 790\,\text{nm}$ (Sample 3), $\lambda_{\text{em}} = 800\,\text{nm}$ (Sample 1).

7.2.2 Excitation at $\lambda = 532\,\text{nm}$

Fig. 35a shows the PL spectra of the samples in the wavelength range of $500-820\,\text{nm}$ with the excitation wavelength of $\lambda_{\text{exc}} = 532\,\text{nm}$. The same spectra are again shown in Fig. 35b in smaller wavelength range in order to see the shapes of the spectra more clearly. As can be seen in this figure, the PL is obtained at the wavelength of $\lambda_{\text{em}} = 800\,\text{nm}$ in the Samples 2 and 3, whereas no signal can be seen from the Sample 1 in this wavelength regime. Moreover, this signal is very strong in the case of the Sample 2. The release of energy at 800 nm can be related to the transition $3 \rightarrow 0$ via nonradiative transitions $5 \rightarrow 4 \rightarrow 3$ in the same way as was the case in the previous subsection.

After the PL spectra of the samples were measured at visible wavelengths, the PL was studied at NIR wavelengths using the PL-setup that was described in Section 5.3. The samples were placed on the sample holder and the pump power was set to 1.5 W. When the sensitivity of the system was optimized, the samples were measured first in the wavelength range of $900 - 1000\,\text{nm}$ and then in the range of $1400 - 1600\,\text{nm}$. No emission via the transition $2 \rightarrow 0$ was observed in the former case. However, smooth signals were obtained in the latter case. Fig. 36 shows the measured PL-signals as a function of the wavelength. The signals were normalized to the maximum value that was obtained during the measurements. As can be seen in Fig. 36, a wide spectrum peaked at approximately $\lambda = 1534\,\text{nm}$ is obtained from all the samples. This wavelength corresponds to the most important transition

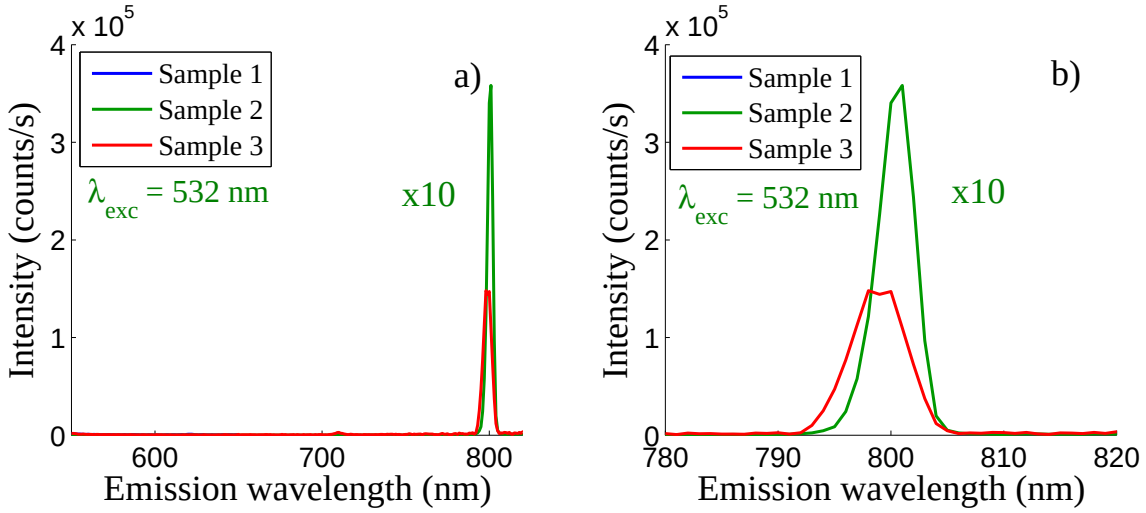

Figure 35: PL spectra of the samples at a) $560 - 820\,\mathrm{nm}$ and b) $780 - 820\,\mathrm{nm}$ with $\lambda_{\mathrm{exc}} = 532\,\mathrm{nm}$. The intensity from the Sample 2 has been reduced by a factor of 10.

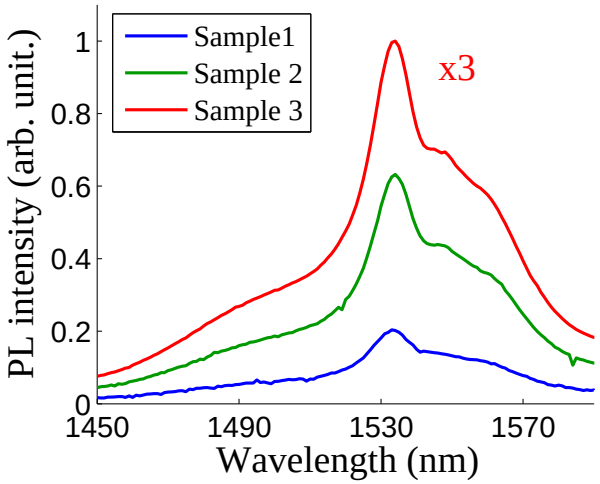

Figure 36: PL spectra of the samples at $1450 - 1590\,\mathrm{nm}$ with $\lambda_{\mathrm{exc}} = 532\,\mathrm{nm}$. The intensity from the Sample 3 has been reduced by a factor of 3.

$1 \rightarrow 0$ in the Er-ions. The shape of the spectrum is very similiar to the one measured from a typical Er-doped samples, as was presented in Fig. 8 and reported before [30, 67, 68, 69, 70]. Moreover, the signal is much stronger in the Sample 3 than in the Samples 1 and 2. This clearly indicates that the PL intensity of the $1 \rightarrow 0$ transition increases dramatically when the vertical distance between the adjacent Er-ions is increased.

7.3 Up-conversion

In the third part of this chapter, up-conversion of light was studied using two excitation wavelengths, $\lambda_{exc} = 800\,nm$ and $\lambda_{exc} = 980\,nm$. These wavelengths correspond to the transitions $0 \rightarrow 3$ and $0 \rightarrow 2$ in the Er-ions, respectively. The former case was studied first.

7.3.1 Excitation at $\lambda = 800\,nm$

Fig. 37a shows the PL spectra of the samples at $460 - 700\,nm$ with the excitation wavelength of $\lambda_{exc} = 800\,nm$. Fig. 37b shows the same spectra in a smaller wavelength regime to clearly distinguish the differences between each sample. Fig. 37a

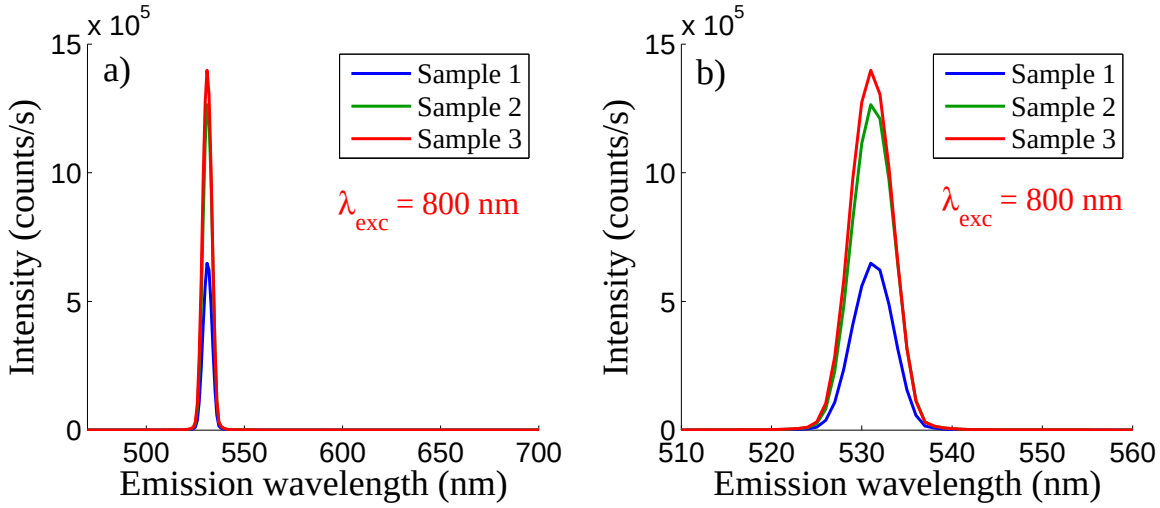

Figure 37: PL spectra of the samples at a) $460 - 700\,nm$ and b) $510 - 560\,nm$ with $\lambda_{exc} = 800\,nm$.

shows that a strong signal peaked at 532 nm is observed in all the samples. This, in turn, corresponds to the transition $5 \rightarrow 0$. There are two ways how this state could have been reached with the pump wavelength of 800 nm. In the first case, the electrons are excited to the band 3 via the pump transition $0 \rightarrow 3$, where they decay nonradiatively to the band 2 and then to the band 1 via the transitions $3 \rightarrow 2 \rightarrow 1$. Because of the long lifetime of the band 1, a moderate population of electrons is most likely generated in this state. The electrons in this state then absorb the pump photons again and excite to the band 5 via the excited state absorption $1 \rightarrow 5$. From the band 5, the electrons then decay radiatively to the ground state via the transition $5 \rightarrow 0$, generating photons with the emission wavelength of 532 nm, which is observed in the PL measurement. This process is illustrated in Fig. 38a.

The state 5 can also be reached in a different way: the electrons are first excited from the band 0 to the band 3 by absorbing the pump photons with $\lambda_{exc} = 800\,nm$. The excited electrons then decay radiatively or nonradiatively to the band 2. This state also has somewhat long lifetime ($\sim 100\,\mu s$), thus, the electrons remain in this state for this designated amount of time. During this time, energy-transfer between

the adjacent Er-ions occurs and as a result, some electrons are excited to the band 6 via the ETU2 process that was described in Section 3.2. When the electrons reach the band 6, they decay to the band 5 and then to the band 0 via the transition $5 \rightarrow 0$, generating light with the emission wavelength of $\lambda_{\text{em}} = 532\,\text{nm}$. However, this process is very unlikely. Even if the electrons could make the transition to the band 6, the energy is most likely lost via the transition $6 \rightarrow 1$ as was observed in the previous subsection. This process is illustrated in Fig. 38b.

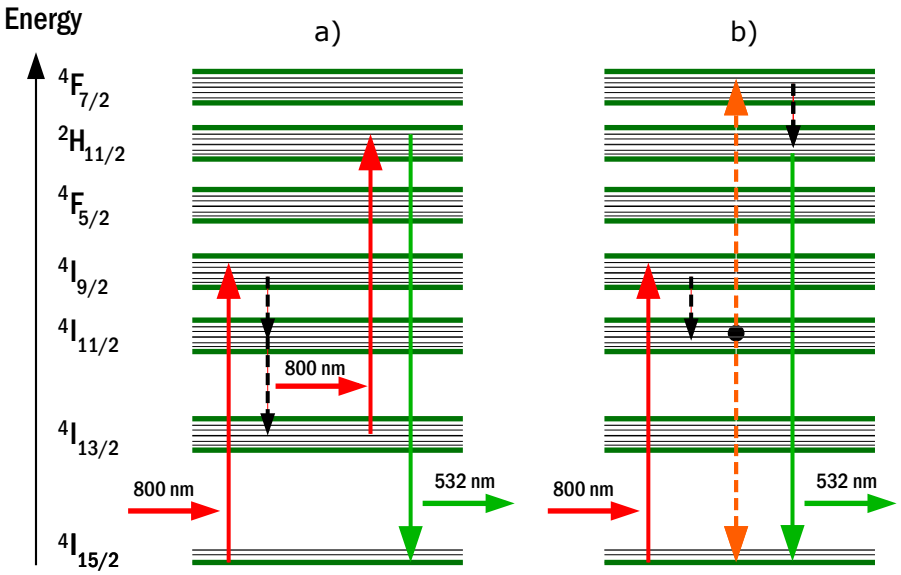

Figure 38: Two possible energy-transfer up-conversion processes for 800 nm $\rightarrow$ 532 nm.

Nevertheless, the signal that was observed during the measurement is approximately two times higher in the Samples 2 and 3 than in the Sample 1. The reason for this cannot be confirmed but it is likely that the rate of absorption at 800 nm in the Samples 2 and 3 are stronger compared to the Sample 1. These results are also in a good agreement with Kasuya *et al.* [66] who observed up-conversion of light at $\lambda_{\text{em}} = 560\,\text{nm}$ using the same excitation wavelength as here. However, in their case, the emission occurs from the $^4S_{3/2}$ state, whereas the emission in this work occurs from the $^2H_{11/2}$ state.

7.3.2 Excitation at $\lambda = 980\,\text{nm}$

After the study of the energy-transfer up-conversion of the samples at $\lambda_{\text{exc}} = 800\,\text{nm}$, the measurements were repeated by changing the excitation wavelength to $\lambda_{\text{exc}} = 980\,\text{nm}$. Fig. 39a shows the results in the wavelength range of $460 - 800\,\text{nm}$ and Fig. 39b in the wavelength range of $460 - 660\,\text{nm}$ for a closer look of the data.

Two peaks centered at approximately 488 nm and 651 nm are now observed. These wavelengths can be related to the transitions $6 \rightarrow 0$ and $4 \rightarrow 0$, respectively. The former of these states can be reached with the transitions $0 \rightarrow 2 \rightarrow 6$ via

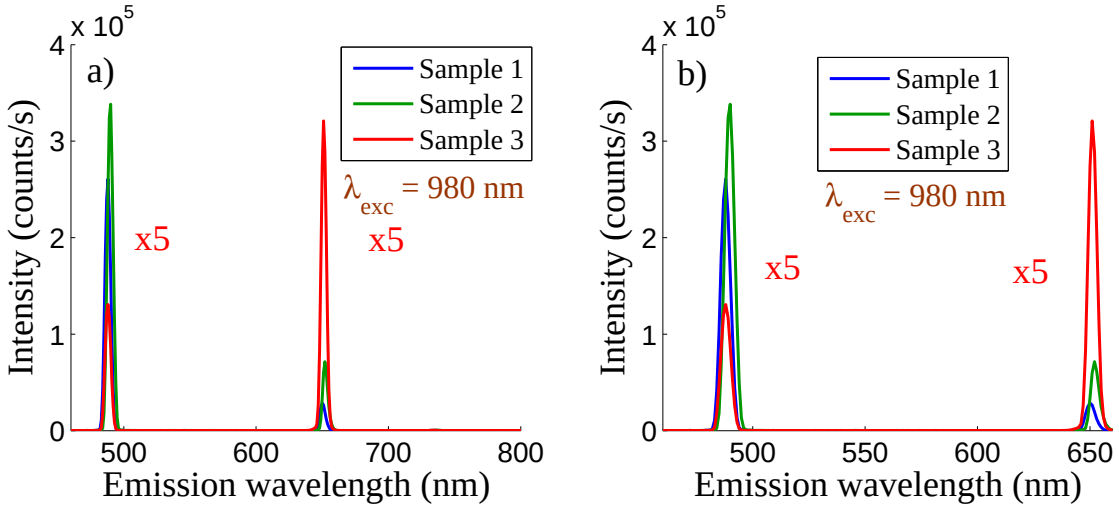

Figure 39: PL spectra of the samples at a) $460 - 800\,\text{nm}$ and b) $460 - 660\,\text{nm}$ with $\lambda_{\text{exc}} = 980\,\text{nm}$.

the excited state absorption process; the latter is reached with either radiative or nonradiative transition from the band 6 to the band 5 and then to the band 4 or directly from the band 6 to the band 4. These processes are illustrated more clearly in Figs. 40a and Fig. 40b, respectively. The PL appears to be much stronger in

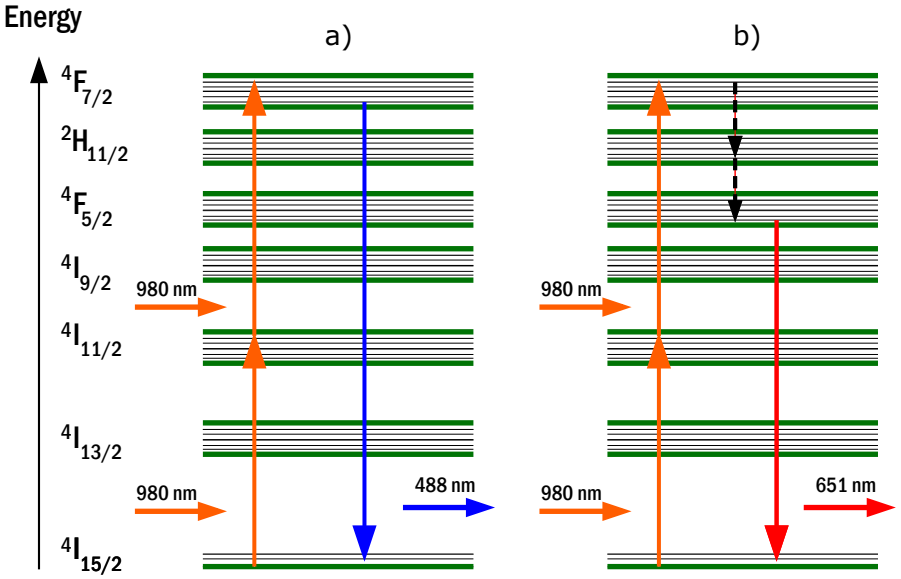

Figure 40: Possible energy-transfer up-conversion processes for a) 980 nm → 488 nm and b) 980 nm → 651 nm.

the Sample 3 than in the Samples 1 or 2. The reason may, again, be the higher absorption rate of photons at $\lambda = 980\,\text{nm}$ in the Sample 3. Up-conversion in the Er-ions at $\lambda_{\text{em}} = 650\,\text{nm}$ with $\lambda_{\text{exc}} = 980\,\text{nm}$ has also been reported before [44, 71, 72]. Thus, these publications support the results obtained here.

To sum up, the absorption and emission measurements in this chapter have shown many interesting features from the samples. Firstly, it was noticed that the Sample 1 that contains only Er_2O_3 is a poor emitter in every aspect compared to the other samples. This can be related to the fact that there is no suitable host material for the Er-ions in Er_2O_3 that could fulfill the required criteria that were discussed in Section 3.4. The Samples 2 and 3, in turn, are clearly better emitters in both the visible and NIR spectrum of light because the Er-ions are doped to Al_2O_3 which is an excellent host material. When one is interested in the amplification of light at around $1.55\,\mu$m, Sample 3 offers much stronger emission than the Sample 2. The Sample 3 can also be used to up-convert light more efficiently with either $\lambda_{\text{exc}} = 800\,\text{nm}$ or $\lambda_{\text{exc}} = 980\,\text{nm}$ as the excitation wavelengths, respectively. Although it was found unusual that the increase in the vertical distance between the Er-ions in the Samples 2 and 3 increased the up-conversion properties of the samples, the higher rate of absorption in the Samples 2 and 3 was considered as the reason for this increase.

8 Summary and outlook

In this thesis, the importance of erbium as a gain material in the optical amplifiers was explained and the unique optical properties of erbium were discussed. The detrimental transitions that limit the operation of Er-doped amplifiers were described and it was shown that these unwanted processes become very important when the Er-ions are integrated with waveguide amplifiers where the amplification of light must be generated in small structures and in short propagation distances. It was argued that in order to reduce these unwanted processes and to ensure the best possible operation of the Er-doped waveguide amplifiers, new methods and fabrication techniques are needed. Several fabrication techniques that are able to produce Er-doped materials were mentioned and of these methods, the focus was on ALD because of its unique deposition properties. The operation principle as well as the advantages and disadvantages of ALD were examined.

The goal of this thesis was to develop an ALD process for erbium oxide (Er_2O_3) by using oxygen (O_2) plasma and tris(2,2,6,6-tetramethyl-3,5-heptanedionato) erbium ($Er(thd)_3$) as the precursors in the deposition. In the process development, the deposition temperature of the process, the temperature, flow rate, pulse and purge times of the $Er(thd)_3$ precursor as well as the O_2 plasma exposure time and power were optimized one at a time. The optimized deposition parameters of the Er_2O_3 process are shown in Table 11. With the optimized values, the growth rate of 0.215

Table 11: The ALD parameters of the optimized Er_2O_3 process.

Dep./Source Temp.	Er pulse / purge time	O_2 pulse / purge time	Er flow rate	O_2 flow rate	Plasma power/time
325/145° C	3.0/6.0 s	13.0/2.0 s	100 sccm	$\sim$ 150 sccm	2500 W/10.0 s

Å/cycle and the non-uniformity of 3.55 % were obtained for Er_2O_3 on 6" wafer, respectively.

Once the Er_2O_3 process development was completed, various Er_2O_3 samples were fabricated for optical property characterization: one single-layer Er_2O_3 sample and two Er_2O_3-Al_2O_3 samples. In the Er_2O_3-Al_2O_3 samples, the thickness of the Al_2O_3 was varied. The as-deposited samples were then optically characterized with absorption and photoluminescence measurements and it was observed that the photoluminescence at the most important wavelength $\lambda = 1.53\,\mu$m was enhanced in the Er_2O_3-Al_2O_3 samples and moreover, when the thickness of the Al_2O_3-layer was increased. The enhanced photoluminescence signal in the Er_2O_3-Al_2O_3 samples was caused by the presence of Al_2O_3 because Al_2O_3 is an excellent host material for the Er-ions. Furthermore the enhancement of the photoluminescence signal as the thickness of the Al_2O_3 was increased was most likely caused by the increased distance between the adjacent Er-ions in the samples due to the reduced ion-ion interaction processes.

To sum up, this thesis showed that the plasma-enhanced ALD is an excellent tool to fabricate Er-doped materials and to control the profile of the Er-ions and,

thus, the photoluminescence of the deposited samples.

Although this thesis showed that the plasma-enhanced ALD can be used to fabricate Er-doped materials and to control their photoluminescence, more knowledge is needed if one wants to implement these materials in the real amplifier devices. For example, it is mandatory to know the lifetime of the first excited state in the Er-ions in order to achive reasonable gain in the amplifier. Moreover, the concentration of the Er-ions in the samples and the absolute value of the maximum achievable gain of the Er-doped Al_2O_3 samples has to be known. Therefore, much more work is required in the future in order to instrument the materials fabricated in this thesis with optical waveguides.

References

[1] B. E. A. Saleh and M. C. Teich, *Fundamentals of photonics*, 2nd ed. Wiley-Interscience, 2007.

[2] B. Eggleton, L.-D. Barry, and K. Richardson, "Chalcogenide Photonics," *Nature Photonics*, vol. 5, no. 12, 2011.

[3] F. Mitschke, *Fiber Optics*, 1st ed. Springer Science & Business Media, 2010.

[4] Govind P. Agrawal, *Fiber-Optic Communications Systems*, 4th ed. Wiley, 2010.

[5] M. Norouzi, P. Badeka, P. Chahande, and B. Briley, "A survey on rare earth doped optical fiber amplifiers," *IEEE International Conference on Electro-Information Technology , EIT 2013*, 2013.

[6] A. Kenyon, "Recent developments in rare-earth doped materials for optoelectronics," vol. 26, no. 4-5, 2002.

[7] S. S. Pathmanathan and P. K. Choudhury, *Novel usage of erbium in optical communication systems : from fundamentals to performance characteristics*, 1st ed. Nova Science, 2010.

[8] I. Trabelsi, R. Maâlej, M. Dammak, a. Lupei, and M. Kamoun, "Crystal field analysis of Er^{3+} in Sc_2O_3 transparent ceramics," *Journal of Luminescence*, vol. 130, no. 6, 2010.

[9] P. C. Becker, N. A. Olsson, and J. R. Simpson, *Erbium-doped fiber amplifiers : fundamentals and technology.* Academic Press, 1999.

[10] F. Priolo, T. Gregorkiewicz, M. Galli, and T. F. Krauss, "Silicon nanostructures for photonics and photovoltaics." *Nature nanotechnology*, vol. 9, no. 1, 2014.

[11] J. Bradley and M. Pollnau, "Erbium-doped integrated waveguide amplifiers and lasers," *Laser & Photonics Reviews*, vol. 5, no. 3, 2011.

[12] P. G. Kik and A. Polman, "Erbium doped optical waveguide amplifiers on silicon," *MRS Bulletin*, vol. 37, no. 9, 1998.

[13] P. G. Kik, "Energy transfer in erbium doped optical waveguides based on silicon," Doctoral dissertation, FOM-Institute for Atomic and Molecular Physics, 2000.

[14] G. N. van den Hoven, E. Snoeks, a. Polman, C. van Dam, J. W. M. van Uffelen, and M. K. Smit, "Upconversion in Er-implanted Al_2O_3 waveguides," *Journal of Applied Physics*, vol. 79, no. 3, 1996.

[15] J. Päiväsaari, M. Putkonen, T. Sajavaara, and L. Niinistö, "Atomic layer deposition of rare earth oxides: erbium oxide thin films from β-diketonate and ozone precursors," *Journal of Alloys and Compounds*, vol. 374, no. 1-2, 2004.

[16] N. Mais, J. P. Reithmaier, A. Forchel, M. Kohls, L. Spanhel, and G. Müller, "Er doped nanocrystalline ZnO planar waveguide structures for 1.55 μm amplifier applications," *Applied Physics Letters*, vol. 75, no. 14, 1999.

[17] K. Hattori, T. Kitagawa, M. Oguma, Y. Ohmori, and M. Horiguchi, "Erbium-doped silica-based waveguide amplifier integrated with a 980/1530 nm wdm coupler," *Electronics Letters*, vol. 30, no. 11, 1994.

[18] X. Multone, Y. Luo, and P. Hoffmann, "Er-doped Al_2O_3 thin films deposited by high-vacuum chemical vapor deposition (HV-CVD)," *Materials Science and Engineering: B*, vol. 146, no. 1–3, 2008.

[19] M. Mahnke, S. Wiechmann, H. J. Heider, O. Blume, and J. Müller, "Aluminum Oxide Doped with Erbium, Titanium and Chromium for Active Integrated Optical Applications," *International Journal of Electronics and Communications*, vol. 55, no. 5, 2001.

[20] R. Serna, J. M. Ballesteros, M. de Castro, J. Solis, and C. N. Afonso, "Optically active Er–Yb doped glass films prepared by pulsed laser deposition," *Journal of Applied Physics*, vol. 84, no. 4, 1998.

[21] J. D. B. Bradley, M. C. e Silva, M. Gay, L. Bramerie, A. Driessen, K. Wörhoff, J.-C. Simon, and M. Pollnau, "170 Gbit/s transmission in an erbium-doped waveguide amplifier on silicon," *Opt. Express*, vol. 17, no. 24, 2009.

[22] J. Shmulovich, A. J. Bruce, G. Lenz, P. B. Hansen, T. N. Nielsen, D. J. Muehlner, G. A. Bogert, I. Brener, E. J. Laskowski, A. Paunescu, I. Ryazansky, D. C. Jacobson, and A. E. White, "Integrated planar waveguide amplifier with 15 dB net gain at 1550 nm," in *Optical Fiber Communication Conference and the International Conference on Integrated Optics and Optical Fiber Communication*. Optical Society of America, 1999.

[23] X. Orignac, D. Barbier, X. M. Du, R. M. Almeida, O. McCarthy, and E. Yeatman, "Sol–gel silica/titania-on-silicon Er/Yb-doped waveguides for optical amplification at 1.5 μm," *Optical Materials*, vol. 12, no. 1, 1999.

[24] A. Q. Le Quang, R. Hierle, J. Zyss, I. Ledoux, G. Cusmai, R. Costa, A. Barberis, and S. M. Pietralunga, "Demonstration of net gain at 1550nm in an erbium-doped polymersingle mode rib waveguide," *Applied Physics Letters*, vol. 89, no. 14, 2006.

[25] S. W. Roberts, G. J. Parker, and M. Hempstead, "The photoluminescence of erbium-doped silicon monoxide," *Optical Materials*, vol. 6, no. 1–2, 1996.

[26] M. Ritala, K. Kukli, A. Rahtu, P. I. Räisänen, M. Leskelä, T. Sajavaara, and J. Keinonen, "Atomic Layer Deposition of Oxide Thin Films with Metal Alkoxides as Oxygen Sources," *Science*, vol. 288, no. 5464, 2000.

[27] L. Karvonen, A. Säynätjoki, Y. Chen, H. Jussila, J. Rönn, M. Ruoho, T. Alasaarela, S. Kujala, R. A. Norwood, N. Peyghambarian, K. Kieu, and S. Honkanen, "Enhancement of the third-order optical nonlinearity in ZnO/Al_2O_3 nanolaminates fabricated by atomic layer deposition," *Applied Physics Letters*, vol. 103, no. 3, 2013.

[28] A. Säynätjoki, L. Karvonen, T. Alasaarela, X. Tu, T. Y. Liow, M. Hiltunen, A. Tervonen, G. Q. Lo, and S. Honkanen, "Low-loss silicon slot waveguides and couplers fabricated with optical lithography and atomic layer deposition," *Optics Express*, vol. 19, no. 27, 2011.

[29] R. Xu, Q. Tao, Y. Yang, and C. G. Takoudis, "Atomic layer deposition and characterization of stoichiometric erbium oxide thin dielectrics on Si(100) using $Er(CpMe)_3$ precursor and ozone," *Applied Surface Science*, vol. 258, no. 22, 2012.

[30] T. T. Van and J. P. Chang, "Controlled erbium incorporation and photoluminescence of Er-doped Y_2O_3," *Applied Physics Letters*, vol. 87, no. 1, 2005.

[31] B. T. Blanquart, M. Kaipio, J. Niinistö, M. Gavagnin, V. Longo, L. Blanquart, C. Lansalot, W. Noh, H. D. Wanzenböck, M. Ritala, and M. Leskelä, "Cyclopentadienyl Precursors for the Atomic Layer Deposition of Erbium Oxide Thin Films," vol. 20, 2014.

[32] H. B. Profijt, S. E. Potts, M. C. M. van de Sanden, and W. M. M. Kessels, "Plasma-Assisted Atomic Layer Deposition: Basics, Opportunities, and Challenges," *Journal of Vacuum Science & Technology A: Vacuum, Surfaces, and Films*, vol. 29, no. 5, 2011.

[33] R. Harris, *Modern physics*, 2nd ed. San Francisco, CA :: Pearson Addison-Wesley, 2008. [Online]. Available: https://teemu-tomcat.linneanet.fi/vwebv/holdingsInfo?bibId=614760

[34] R. L. Liboff, *Introductory quantum mechanics*, 4th ed. Addison-Wesley, 2003.

[35] O. Svelto, *Principles of lasers*, 5th ed. Springer, 2010.

[36] H. Ibach and H. Lüth, *Solid-state physics : an introduction to principles of materials science*, 4th ed. Springer, 2009.

[37] S. G. Lipson, H. Lipson, and D. S. Tannhauser, *Optical physics*, 4th ed. Cambridge University Press, 2009.

[38] S. Hooker and C. Webb, *Laser Physics*. OUP Oxford, 2010.

[39] P.-A. Hansen, H. Fjellvå g, T. Finstad, and O. Nilsen, "Structural and optical properties of lanthanide oxides grown by atomic layer deposition (Ln = Pr, Nd, Sm, Eu, Tb, Dy, Ho, Er, Tm, Yb)." *Dalton transactions*, vol. 42, no. 30, 2013.

[40] Igoscience, "The periodic table of the elements." [Online]. Available: http://igoscience.com/periodic-table-of-elements-free-pdf/

[41] N. Avram and M. G. Brik, *Optical properties of 3d-ions in crystals : spectroscopy and crystal field analysis*, 1st ed. Springer, 2013.

[42] E. Hemmer, N. Venkatachalam, H. Hyodo, A. Hattori, Y. Ebina, H. Kishimoto, and K. Soga, "Upconverting and NIR emitting rare earth based nanostructures for NIR-bioimaging." *Nanoscale*, vol. 5, no. 23, 2013.

[43] X. Qiao, X. Fan, and M. Wang, "Luminescence behavior of Er^{3+} in glass ceramics containing BaF_2 nanocrystals," *Scripta Materialia*, vol. 55, no. 3, 2006.

[44] R. Narro-García, E. Chillcce, L. Barbosa, E. de Posada, M. Arronte, and E. Rodriguez, "Fabrication and upconversion luminescence of Er^{3+}/Yb^{3+} codoped TeO_2–WO_3–Na_2O–Nb_2O_5–Al_2O_3 glass fibers," *Journal of Luminescence*, vol. 134, 2013.

[45] A. Polman, "Absorption and emission spectroscopy in Er^{3+}-Yb^{3+} doped aluminum oxide waveguides," vol. 21, 2003.

[46] M. C. Pujol, J. J. Carvajal, X. Mateos, P. Formentín, J. Pallarès, L. F. Marsal, K. H. Park, F. Rotermund, K. Kim, M. Aguiló, and F. Díaz, "New microarchitectures of (Er, Yb): Lu_2O_3 nanocrystals embedded in PMMA : synthesis, structural characterization, and luminescent properties," 2013.

[47] A. Yariv, P. Yeh, and A. Yariv, *Photonics : optical electronics in modern communications*, 6th ed. Oxford University Press, 2007.

[48] T. Suntola, "Atomic layer epitaxy," *Materials Science Reports*, vol. 4, no. 5, 1989.

[49] S. M. George, "Atomic layer deposition: an overview." *Chemical reviews*, vol. 110, no. 1, 2010.

[50] R. W. Johnson, A. Hultqvist, and S. F. Bent, "A brief review of atomic layer deposition: from fundamentals to applications," *Materials Today*, vol. 17, no. 5, 2014.

[51] M. de Keijser and C. van Opdorp, "Atomic layer epitaxy of gallium arsenide with the use of atomic hydrogen," *Applied Physics Letters*, vol. 58, no. 11, 1991.

[52] M. A. Lieberman and A. J. Lichtenberg, *Principles of plasma discharges and materials processing*, 2nd ed. John Wiley & Sons, 2005.

[53] M. Di Ventra, S. Evoy, and J. J. R. Helfin, *Introduction to Nanoscale Science and Technology*, 1st ed. Kluwer Academic Publishers, 2004.

[54] L. Karvonen, A. Säynätjoki, Y. Chen, H. Jussila, J. Rönn, M. Ruoho, T. Alasaarela, S. Kujala, R. A. Norwood, N. Peyghambarian, K. Kieu, and S. Honkanen, "Enhancement of the third-order optical nonlinearity in ZnO/Al_2O_3 nanolaminates fabricated by atomic layer deposition," *Applied Physics Letters*, vol. 103, no. 3, 2013.

[55] T. Alasaarela, "Atomic layer deposited titanium dioxide in optical waveguiding applications," Doctoral dissertation, Aalto university, 2011.

[56] J. Päiväsaari, J. Niinistö, K. Arstila, K. Kukli, M. Putkonen, and L. Niinistö, "High Growth Rate of Erbium Oxide Thin Films in Atomic Layer Deposition from $Er(CpMe)_3$ and Water Precursors," *Chemical Vapor Deposition*, vol. 11, no. 10, 2005.

[57] Picosun, "PICOSUN™ R-series Atomic Layer Deposition (ALD) reactors." [Online]. Available: http://www.picosun.com/en/products/picosun8482+r-series/

[58] D. K. Schroder, *Semiconductor material and device characterization*, 3rd ed. IEEE Press, 2006.

[59] R. M. A. Azzam, "Determination of the complex dielectric function of an unbacked or embedded thin film by grazing-incidence reflection or transmission ellipsometry," *Optics Communications*, vol. 80, no. 2, 1990.

[60] Pti-nj, "QuantaMaster™ 40 Steady State Spectrofluorometer." [Online]. Available: http://www.pti-nj.com/flyers/QM-40.pdf

[61] J. Hassinen, "private communication," 2014.

[62] R. D. Shannon, "Refractive Index and Dispersion of Fluorides and Oxides," *Journal of Physical and Chemical Reference Data*, vol. 31, no. 4, 2002.

[63] S. Q. Man, E. Y. B. Pun, and P. S. Chung, "Upconversion luminescence of Er^{3+} in alkali bismuth gallate glasses," *Applied Physics Letters*, vol. 77, no. 4, 2000.

[64] H. Lin, E. Y. B. Pun, S. Q. Man, and X. R. Liu, "Optical transitions and frequency upconversion of Er^{3+}-ions in Na_2O-$Ca_3Al_2Ge_3O_{12}$-glasses," vol. 18, no. 5, 2001.

[65] M. Środa, K. Szlósarczyk, M. Różański, M. Sitarz, and P. Jeleń, "Spectroscopic properties of transparent Er-doped oxyfluoride glass-ceramics with GdF," *Spectrochimica acta. Part A, Molecular and biomolecular spectroscopy*, vol. 134, 2015.

[66] a. Kasuya and M. Suezawa, "Resonant excitation of visible photoluminescence from an erbium-oxide overlayer on Si," *Applied Physics Letters*, vol. 71, no. 19, 1997.

[67] R. Narro-García, E. F. Chillcce, a. R. Miranda, J. M. Giehl, L. C. Barbosa, E. Rodriguez, and M. Arronte, "Optical and physical properties of Er^{3+}-Yb^{3+} co-doped tellurite fibers," vol. 8120, 2011.

[68] R. Guo, B. Wang, X. Wang, L. Wang, L. Jiang, and Z. Zhou, "Optical amplification in Er/Yb silicate slot waveguide." *Optics letters*, vol. 37, no. 9, 2012.

[69] S. Horikanena, T. Ohtsukia, S. Jiang, N. Peyghambariana, H. Head, and E. Polytechnique, "High Er concentration phosphate glasses for planar waveguide amplifiers," vol. 2996.

[70] K. Solehmainen, M. Kapulainen, and K. Polamo, "Erbium-Doped Waveguides Fabricated With Atomic Layer Deposition Method," vol. 16, no. 1, 2004.

[71] L. Luo, F. Song, X. Yu, W. Wang, C. Ming, L. Han, Y. Yu, H. Wu, and J. Tian, "Intense 1.54 μm fluorescence of Er^{3+}/Yb^{3+}-codoped phosphate glass and the three-photon phenomenon of near infrared upconversion luminescence," *Journal of Applied Physics*, vol. 107, no. 3, 2010.

[72] F. Song, G. Zhang, M. Shang, H. Tan, J. Yang, and F. Meng, "Three-photon phenomena in the upconversion luminescence of erbium–ytterbium-codoped phosphate glass," *Applied Physics Letters*, vol. 79, no. 12, 2001.